THE MAGNETOTELLURIC PHASE TENSOR METHOD FOR IMAGING THE NORTH ANATOLIAN FAULT ZONE

by

Ekrem Bekin

B.S., Geophysical Engineering, Istanbul University, 2012

Submitted to Kandilli Observatory and Earthquake
Research Institute in partial fulfillment of the
requirements for the degree of
Master of Science

Graduate Program in Geophysics
Boğaziçi University
2016

THE MAGNETOTELLURIC PHASE TENSOR METHOD FOR IMAGING THE NORTH ANATOLIAN FAULT ZONE

APPROVED BY:

Assoc. Prof. Dr. Sabri Bülent Tank
(Thesis Supervisor)

Prof.Dr. Mustafa Aktar

Prof.Dr.Aysan Gürer (IU)

DATE OF APPROVAL: 25.04.2016

ACKNOWLEDGEMENTS

I would first like to thank my thesis advisor Assoc. Prof. Dr. Sabri Bülent Tank for allowing this paper to be my own work and steered me in the right direction whenever he thought I needed it. His ideas for my improvement are very precious.

I would also like to thank Mrs. Elif Tolak Çiftçi. I am gratefully indebted to her for her very valuable comments. I would like to acknowledge Berk Yakar and Özlem Cengiz for their assitance from the beginning of my master program. I would also like to thank Rıdvan Örsvuran, Deniz Ertuncay and Sinan Özaydın for their valuable comments during my study.

Finally, I must express my profound gratitude to my family and to my friends for providing me with unfailing support and continuous encouragement throughout my years of study and through the process of researching and writing this thesis. This accomplishment would not have been possible without them. Thank you.

ABSTRACT

THE MAGNETOTELLURIC PHASE TENSOR METHOD FOR IMAGING THE NORTH ANATOLIAN FAULT ZONE

Magnetotelluric data often suffer from localized (three-dimensional) heterogeneities by a real and frequency independent phenomenon known as “galvanic distortions”. There have been numerous techniques developed for avoiding the galvanic distortions and thus, determining the dimensionality of the observed data. Groom and Bailey’s decomposition and the phase tensor analyses are used for avoiding galvanic distortions and Swift’s analysis, Bahr’s parameters are some of the most common and conventional dimensionality determination approaches. The phase tensor is a relatively more recent approach compared to the rest and is useful for studying in a distortion-free medium. The main objective of this study is to develop MATLAB® scripts for calculating and imaging the phase tensor ellipses and applying them to observed data collected at the central part of the North Anatolian Fault Zone (NAFZ). Final images are compared to other geophysical study results performed within the same area.

ÖZET

MANYETOTELLÜRİK FAZ TENSÖRÜ METODU KULLANARAK TOSYA ÇEVRESİNDE KUZEY ANADOLU FAYI'NIN GÖRÜNTÜLENMESİ

Manyetotellürik veri, çoğu kez "galvanik bozulma" olarak bilinen lokalize olmuş çok boyutlu heterojen yapılardan etkilenir. Galvanik bozulmalar gerçel sayılardan oluşur ve frekanstan bağımsızdır. Galvanik bozulmalar ile ilgilenen ve ayrıca yeraltındaki boyutluluğu kestirmede kullanılan birçok teknik geliştirilmiştir. Groom ve Bailey ayrıştırması ve faz tensörü verideki bozulmadan kurtulmayı sağlayan metotlardandır. Swift'in analizi ve Bahr parametreleri yeraltı yapısının uzanımı hakkında bilgi almayı sağlayan yöntemlerden en yaygın kullanılanlarından bazılarıdır. Faz tensörü diğerlerine göre daha yeni bir yöntemdir ve galvanik düzeltmedeki avantajı ile yeraltındaki yapının boyutluluğu hakkında geleneksel yöntemlere göre daha iyi bilgi vermektedir. Bu çalışmanın temel amacı faz tensörü analizi yapan MATLAB® programları geliştirmek ve bunu Kuzey Anadolu Fay Hattının orta kesiminde toplanan gerçek veriye uygulamaktır. Sonuçlar aynı bölgede yapılmış başka jeofizik çalışmalarla da karşılaştırılmıştır.

TABLE OF CONTENTS

LIST OF FIGURES

LIST OF SYMBOLS

Φ_{ij}	Impedance Phase
B	Magnetic Induction
d	Distortion tensor elements
d	Data parameters
D	Dielectric Displacement
D	2-by-2 frequency independent distortion tensor
det	Determinant of the phase tensor
E	Electric field
$\mathbf{E_R}$	Regional electric field
$\mathbf{E_S}$	Scattered electric field
F	Observation Matrix / Model Response Matrix
H	Magnetic Field
J	Electric current density
m	model parameters
R	Rotation matrix
sec	second(s)
sk	skew of the phase tensor
T	Transfer Function (Induction Arrow)
tr	Trace of the phase tensor
X	Impedance real part tensor
$\mathbf{X_R}$	Regional impedance real part tensor
Y	Impedance imaginary part tensor
$\mathbf{Y_R}$	Regional impedance imaginary part tensor
Z	Magnetotelluric impedance tensor

α	Coordinate dependent parameter (angle) of the phase tensor ellipse
β	Skew angle of the phase tensor ellipse
δ	Skin depth
ε	Electric Permittivity
κ	Swift's (Conventional) Skew
μ	Magnetic permeability
μ_0	Magnetic permeability of free space
$\boldsymbol{\varphi}$	Phase Tensor
φ_{max}	Major axis of the phase tensor ellipse
φ_{min}	Minor axis of the phase tensor ellipse
ρ	Electric charge density
ρ_e	Free electric charge
ρ_a	Apparent Resistivity
σ	Electric Conductivity
θ	Geoelectric Strike (Swift)
$\boldsymbol{\omega}$	Angular frequency

LIST OF ACRONYMS/ ABBREVIATIONS

1-D	One dimensional
2-D	Two dimensional
3-D	Three dimensional
TE	Transverse Electric
TM	Transverse Magnetic
AFZ	Almus Fault Zone
CAFZ	Central Anatolian Fault Zone
CPS	Central Pontide Supercomplex
ÇKFZ	Çerkeş-Kurşunlu Fault Zone
DFZ	Dodurga Fault Zone
EFZ	Eldivan Fault Zone (in general fault map)
EFZ	Ekinveren Fault Zone (in field/case study)
ESFZ	Ezinepazarı-Sungurlu Fault Zone
ETGFZ	Eskişehir-Tuzgölü Fault Zone
KFZ	Kızılırmak Fault Zone
LFZ	Laçin Fault Zone
NAFZ	North Anatolian Fault Zone
ODFZ	Orta-Devrez Fault Zone
TVZ	Taupo Volcanic Zone

1. INTRODUCTION

The main goal in geophysics is to investigate the physical properties of the Earth and its subsurface. For this purpose, several methods sensitive to various physical parameters were developed. One of these methods is a geo-electromagnetic technique known as magnetotellurics method (Vozoff, 1972; Chave and Jones, 2012). Magnetotellurics (MT) method is based on monitoring the electric and magnetic fields as time series at the surface of the Earth. Following the data acquisition, electromagnetic data are transferred to frequency domain and electromagnetic impedance elements are calculated for further analyses and numerical modeling.

MT data often suffer from localized (three-dimensional) subsurface heterogeneities by surplus effects known as “galvanic distortions”. They are real and frequency independent. There have been numerous attempts made to remove these distortions from observed data (Vozoff, 1972; Bahr, 1988; 1991; Groom &Bailey, 1989; Caldwell et al., 2004; Bibby et al., 2005). In general, this operation can be considered as part of the dimensionality analysis and it targets to assist the determination of the distortion-free impedance tensor and regional distortion-free geo-electric strike (Vozoff, 1991; Bahr, 1988; Groom and Bailey, 1989; Mc Neice and Jones, 2001; Caldwell et al., 2004; Bibby et al., 2005).

To discard the effects of galvanic distortions from their data, MT practitioners have endeavored to produce more accurate subsurface models with several common approaches such as: Swift’s analysis (Swift, 1967), Bahr’s parameters (Bahr, 1988), Groom and Bailey’s decomposition (Groom and Bailey, 1989) and the MT phase tensors (Caldwell et al., 2004). Swift’s analysis is an amplitude based approach that deals with the recovery of the so-called “geo-electric strike angle” rather than distortion removal. This analysis is performed by maximizing (minimizing) the off - diagonal (diagonal) elements of the impedance tensor (Swift, 1967; Bahr and Simpson, 2005). Bahr’s parameters are calculated form the observed impedance tensor and are used to detect dimensionality, too. The

electromagnetic strike that is recovered using the Bahr's method is often referred to as the phase-sensitive strike (Simpson, 2001; Bahr, 1988; Bahr, 1991; Bahr and Simpson, 2005). In Groom and Bailey's decomposition, the main objective is to separate the local responses that cause galvanic scatterings on the electric field data and regional response parameters as much as possible through a product factorization (Groom and Bailey, 1989). In other words, Groom and Bailey decomposition is used for removing the distortion parameters "twist" and "shear". The method is unable to solve the problems caused by "the site gain" and "the anisotropy" and leave them untouched. Induction arrows can also be used to resolve difficulties in determining the geo-electric strike. The theory of this method depends on linear combinations of horizontal and vertical magnetic field components (Vozoff, 1991).

MT phase tensor is a practical method introduced by Caldwell et al., (2004) and is useful for determining the dimensionality and geo-electric strike of a regional structure. The phase tensor elements may be calculated by taking the ratio of the imaginary and real components of the complex impedance tensor elements (Caldwell et al., 2004). The major advantage of this technique is that, the phase tensor elements do not contain effects caused by galvanic distortions.

Aim of this thesis is to develop MATLAB® scripts that perform phase tensor analysis. Following the development, some synthetic data obtained from several forward subsurface models were applied to the scripts. For this purpose, a three-dimensional forward code developed by Mackie et al., (1993) was used. Firstly, the scripts were tested for a homogenous half-space. An identical geometry (and structure) given in the Caldwell et al. (2004) was used during the tests of the developed scripts (at this point, it might be important to note that Caldwell et al., (2004) used a different three-dimensional forward code developed by Xiong (1992) and Xiong and Tripp (1995) for calculating the model responses).

Finally, after testing the synthetic models, the scripts were used for analyzing an observed MT data set. For this purpose a north-south aligned MT profile was used that

crosses the North Anatolian Fault Zone (near Tosya, Kastamonu). The profile is made up of 25 wide-band (320 Hz - 1800 s) MT soundings.

Chapter 2 briefly explains the theory of the MT method. Within this chapter, concepts of directionality and dimensionality are also mentioned. Swift's analysis (Swift, 1967) and the phase tensors (Caldwell et al., 2004) are described. Chapter 3 involves the development, tests and application of the MATLAB® scripts on sythetic data. A short description of the case study and the application of the scripts on observed data can also be found in Chapter 3. Results and their interpretations are shown in Chapter 4. Detailed information about how the phase tensor ellipses and maps are produced with synthetic (Comparisons to Caldwell et al. (2004) results) and observed data (ellipses superimposed on topography maps and pseudo-sections) can be found in this chapter. Chapter 5 includes discussions and comparisons to other geophysical results. All these information is followed by a conclusion as Chapter 6.

2.THEORY

2.1. BASICS OF MAGNETOTELLURIC (MT) METHOD

2.1.1.Maxwell's Equations

Fundamental theory of electromagnetics and magnetotellurics (MT) method can be described by Maxwell's equations. Maxwell had arranged Gauss, Ampére and Faraday laws to define electromagnetics in a mathematical and physical manner (Ward and Hohmann, 1988). Differential form of Maxwell's equations can be represented as:

$$\nabla \times \mathbf{E} = -\frac{\partial \mathbf{B}}{\partial t} \quad (2.1)$$

$$\nabla \times \mathbf{H} = \mathbf{J} + \frac{\partial \mathbf{D}}{\partial t} \quad (2.2)$$

$$\nabla . \mathbf{D} = \rho \quad (2.3)$$

$$\nabla . \mathbf{B} = 0 \quad (2.4)$$

where **E** is electric field intensity in V/m, **H** is magnetic field intensity in A/m, **B** is magnetic induction in Teslas (Wb/m^2), **J** is the electric current density in A/m^2, **D** is the dielectric displacement ($\mathbf{D} = \varepsilon \mathbf{E}$) in C/$m^2$ and ρ is the electric charge density in C/m^3 (Ward and Hohmann,1988).

2.1.1.1. The Constitutive Relations. The constitutive relations are generally used in electromagnetics in order to define relations between the electric and the magnetic field. For that, the medium should be linear, isotropic and homogeneous. Moreover, the medium should have electrical properties, which are independent of time, temperature or pressure. **B, D** and **J** can be stated as

$$\mathbf{B} = \mu\mathbf{H} \quad (2.5)$$

$$\mathbf{D} = \varepsilon\mathbf{E} \quad (2.6)$$

$$\mathbf{J} = \sigma\mathbf{E} \quad (2.7)$$

where ε is the dielectric permittivity in F/m, μ is the magnetic permeability in H/m (it is assumed to be that of free space $\mu = \mu_0 = 4\pi.10^{-7}$) and σ is the electrical conductivity (in S/m) of the medium (Ward and Hohmann,1988).

If homogeneous Earth materials have conductivity of 10^{-4} S/m or greater, free charge ρ_e scatters in less than 10^{-6} sec. In frequencies less than 10^5 Hz, $\partial\rho_e/\partial t \sim 0$, and by taking the divergence of equation (2.7), we obtain

$$\nabla.\mathbf{J} = 0 \quad (2.8)$$

and this equation does not apply to inhomogeneous regions because at the interface between two distinct media a surface charge accumulates (Ward and Hohmann, 1988).

2.1.2. Assumptions of the MT Method

In the theory of MT method, there are several assumptions so as to understand electromagnetic induction in the Earth (Rikitake, 1948; Tikhonov, 1950; Cagniard, 1953; Keller and Frischknecht, 1966; Bahr and Simpson; 2005).

- In order to apply MT method, Maxwell's equations must be obeyed (Rikitake, 1948; Tikhonov, 1950; Cagniard, 1953).

- Source of the Earth's current is originally external. Thus, most part of the Earth's current is induced by the variation of the external geomagnetic force (Rikitake, 1948).

- In the theory of MT method, the natural electric and magnetic fields of the Earth are measured by the help of the ionospheric current systems. Electromagnetic waves are assumed to be plane waves that penetrate into the Earth near vertical incidence (Cagniard, 1953; Kaufmann and Keller, 1981; Simpson and Bahr, 2005).

- There are also some assumptions on Maxwell's equations. One of them is about Amperé's law, which is

$$\nabla \times \mathbf{H} = \sigma \mathbf{E} - i\omega\varepsilon \mathbf{E} \tag{2.9}$$

where **H** is magnetic field, **E** is electric field, ω angular frequency, σ conductivity and ε dielectric permittivity. At right hand side, the first term is conduction currents and the second term is the displacement currents. Because of the quasistatic approximation, displacement currents are very small when compared with conduction currents. In other words, in the theory of MT method, Amperé's law is assumed to be

$$\nabla \times \mathbf{H} = \sigma \mathbf{E} \tag{2.10}$$

- Another assumption about Maxwell's equations is for Gauss's law for electricity. Original form of the equation is valid for in the static case. That is, source of the electrical field is a charge.

Original form of the equation is:

$$\nabla . \mathbf{E} = \rho \tag{2.11}$$

but the theory of MT method handles the dynamic case of the law. That is, the electric field is related with current flow. In that situation, divergence of the electric field is equal to zero. In MT method, Gauss's law for electricity takes the form as

$$\nabla . \mathbf{E} = 0 \qquad (2.12)$$

(Kaufmann and Keller, 1981; Ward and Hohmann, 1988; Simpson and Bahr, 2005).

- In a multi-dimensional Earth, charge can accumulate along discontinuities. This generates a non-inductive phenomenon known as static shift. Also the Earth behaves as an Ohmic conductor and charge is conserved. That situation obeys the equation

$$\mathbf{J}=\sigma\mathbf{E} \qquad (2.13)$$

where **J** is total electric current density (in Am^{-2}), σ is the conductivity of the sounding medium (in Sm^{-1}) and **E** is the electric field (in Vm^{-1}) (Simpson and Bahr, 2005).

- Changes in the magnetic permeability and electrical permittivity of rocks are assumed negligible compared with changes in bulk rock conductivities (Simpson and Bahr, 2005).

2.1.3. Electromagnetic impedance and impedance tensor

In magnetotelluric studies, there is an interrelation between horizontal components of the electric field (i.e. E_x, E_y) and horizontal components of the magnetic field (i.e. H_x, H_y). It is stated that these components of the electric and the magnetic fields are

proportional to each other and that proportionality is diagnostic for finding different resistivities under the Earth's surface (Tikhonov, 1950; Cagniard, 1953). That is;

$$\mathbf{Z}_{ij} = \frac{E_i}{H_j} \tag{2.14}$$

where **Z** is the electromagnetic impedance (note that electromagnetic impedance is different than electrical impedance) and **E** and **H** are horizontal components of electric and magnetic fields, respectively. Because of **E** and **H** are complex, so the impedance is a complex number. **Z** can also be defined as a tensor (Cagniard, 1953; Swift, 1967; Kaufmann and Keller, 1981, Simpson and Bahr, 2005).

$$\mathbf{Z} = \begin{bmatrix} Z_{11} & Z_{12} \\ Z_{21} & Z_{22} \end{bmatrix} = \begin{bmatrix} E_X/H_X & E_X/H_Y \\ E_Y/H_X & E_Y/H_Y \end{bmatrix} \tag{2.15}$$

2.1.3.1. Dimensionality detection from impedance tensor. If the Earth is one-dimensional (1D), (Swift, 1967; Vozoff, 1991; Simpson and Bahr, 2005) one dimensional electromagnetic impedance tensor takes the form

$$\mathbf{Z}_{1D} = \begin{bmatrix} 0 & Z_{12} \\ -Z_{21} & 0 \end{bmatrix} \tag{2.16}$$

In the two-dimensional (2D) Earth, (Swift, 1967; Vozoff, 1991; Simpson and Bahr, 2005) the 2D electromagnetic impedance tensor is

$$\mathbf{Z}_{2D} = \begin{bmatrix} 0 & Z_{12} \\ Z_{21} & 0 \end{bmatrix} \tag{2.17}$$

In three-dimensional (3D) Earth, impedance elements are neither zero, nor equal (Swift, 1967; Vozoff, 1991; Simpson and Bahr, 2005). Then, 3D impedance tensor takes the form

$$\mathbf{Z}_{3D} = \begin{bmatrix} Z_{11} & Z_{12} \\ Z_{21} & Z_{22} \end{bmatrix} \tag{2.18}$$

2.1.4. Apparent resistivity and impedance phase

Apparent resistivity values are generally seen as curves for displaying results of MT data and this parameter is one of the most frequently used parameter. Cagniard (1953) has proposed two fundamental assumptions for calculating resistivity. Firstly, the Earth should have horizontal layers and each layer should be homogeneous and isotropic. Secondly, magnetic micropulsations should be plane electromagnetic waves running into the Earth. In consideration of these assumptions, Cagniard (1953) has stated that resistivity can be calculated as a function of depth if apparent resistivity is known (Vozoff et al., 1963). Mathematical form of apparent resistivity is given by;

$$\rho_a = \omega\mu_0 \left|\frac{E_X}{H_Y}\right|^2 \tag{2.19}$$

where ρ_a is apparent resistivity in ohm.m, E_X (A.m^{-1}) and H_Y (Wb.m^{-2}) are horizontal components of electric and magnetic fields, respectively, ω and μ_0.

In other words, apparent resistivity can be thought as the average resistivity of the equivalent uniform layered medium (Cagniard, 1953; Simpson and Bahr, 2005).

Another frequently used parameter is the electromagnetic impedance phase. It is already stated that there is an interrelation between horizontal components of the electric field and the magnetic field. These components are proportional to each other and there is a

phase shift between them (Tikhonov, 1950; Kaufmann and Keller, 1981; Vozoff, 1991). It can be represented as

$$\Phi_{ij} = arg(\frac{\mathrm{Im(Zij)}}{\mathrm{Re(Zij)}}) \quad (2.20)$$

where Φ_{ij} is in degrees. Impedance phase is equal to 45° in homogeneous medium because conductivity is stationary everywhere in the medium. Hence, components of the electric and magnetic fields are equal to each other. As long as conductivity of medium increases with depth, the impedance phase increases and becomes larger than 45° and that is also valid for vice versa (Kaufman and Keller, 1981; Vozoff, 1991; Simpson and Bahr, 2005).

2.1.5. Skin Depth

In a uniformly conductive medium, electromagnetic field decays by 1/e (≈ 0.37) (Chave and Jones, 2012). That is, electromagnetic waves diffuse as long as % 67 of their energy is attenuated. This length scale for electromagnetic induction is termed as skin depth (Bedrosian, 2007). Mathematical representation of skin depth is given as

$$\delta(\omega) = \sqrt{\frac{2}{\omega\mu\sigma}} \quad (2.21)$$

In S.I. units, (2.21) can be written as

$$\delta \cong 503\sqrt{\rho T} \quad (2.22)$$

where δ is in meters, T (period) is in seconds and ρ is the electrical resistivity in ohm m. Skin depth formula indicates that, attenuation of electromagnetic waves in conducting

layer is very fast when it is compared with resistive layer. In other words, electromagnetic waves attenuate slowly in a resistive layer (Bedrosian, 2007; Chave and Jones, 2012).

2.2. COPING WITH THE GALVANIC DISTORTIONS

2.2.1 Galvanic Distortion

MT data suffer from galvanic distortions. Distortion of regional electric fields, caused by local structures, is one of the common difficulties faced in the application of the MT method. Galvanic distortion, which is produced by localized heterogeneity on the undistorted (regional) electric field $\mathbf{E_R}$, can be written in the mathematical form as

$$\mathbf{E}(\omega) = \mathbf{E_R}(\omega) + \mathbf{E_S}(\omega), \tag{2.23}$$

where $\mathbf{E}$ is the observed electric field, E_R is the regional electric field, E_S is the secondary electric field, which produced by the interaction of regional conductivity and heterogeneity, and ω is the angular frequency (Caldwell et al., 2004; Bibby et al., 2005).

In theory, inductive effects can be neglected and that the regional electric field $\mathbf{E}_R$ does not change substantially with the lateral extent of the heterogeneity. At this stage, writing the scattered field $\mathbf{E}_S$ as linearly proportional to the regional electric field $\mathbf{E}_R$ may be a good approximation. With these assumptions equation (2.23) may be rewritten in terms of a distortion matrix ($\boldsymbol{D}$), which is a frequency independent linear operator and all components are real, that transforms the regional electric field vector into the distorted field $\mathbf{E}$ observed at the surface (Caldwell et al., 2004). That is:

$$\mathbf{E}(\omega) = \boldsymbol{D}\mathbf{E}_R(\omega), \tag{2.24}$$

where $\boldsymbol{D}$ is the two by two matrix (a second rank, 2-D tensor). The observed electric field can be thought as a linear superposition of the regional field ($\mathbf{E}_R$) and a scattered electric field ($\mathbf{E}_S$) according to equation (2.24). As long as $\boldsymbol{D}$ is real, in a case such that the regional electric field is linearly polarized the distorted electric field is also linearly polarized despite $\mathbf{E}_R$ and $\mathbf{E}_S$ are not usually in the same direction (Caldwell et al., 2004). In a Cartesian coordinate system (x, y) the distortion operator can be written as the matrix

$$\boldsymbol{D} = \begin{bmatrix} d_{11} & d_{12} \\ d_{21} & d_{22} \end{bmatrix} \tag{2.25}$$

where the elements of $\boldsymbol{D}$ depend on the position of the observation point, the shape of the heterogeneity and conductivity of the heterogeneity (Caldwell et al., 2004).

In circumstances where equation (2.24) is valid, the horizontal components of the observed magnetic field $\mathbf{H}$ are equal to the components of the regional magnetic field $\mathbf{H}_R$ (Caldwell et al., 2004; Bibby et al., 2005). That is:

$$\mathbf{H}(\omega) = \mathbf{H}_R(\omega). \tag{2.26}$$

2.2.2 Swift's Analysis

This technique was introduced by Swift (1967). Aim of Swift's (1967) analysis is to determine the geoelectric strike angle of the structure. Swift (1967)'s geoelectric strike can be calculated in numerous ways. Minimizing the sum of the diagonal elements of the impedance tensor leads to:

$$\frac{\partial}{\partial\theta}(|Z_{XX}(\theta)|^2 + |Z_{YY}(\theta)|^2) = 0 \tag{2.27}$$

(likewise, similar to 2.27 it can be calculated by maximizing the off - diagonal elements of the impedance tensor).

$$\frac{\partial}{\partial\theta}(|Z_{XY}(\theta)|^2 + |Z_{YX}(\theta)|^2) = 0 \tag{2.28}$$

This derivation process gives

$$\theta = \frac{1}{4}\frac{(Z_{XX}-Z_{YY})(Z_{XY}+Z_{YX})^* + (Z_{XX}+Z_{YY})^*(Z_{XY}+Z_{YX})}{|Z_{XX}-Z_{YY}|^2+|Z_{XY}+Z_{YX}|^2} \tag{2.29}$$

where Z_{ij}^* is the complex conjugate of Z_{ij} and θ is the geoelectric strike.

This computed strike has 90^o uncertainty in rotation process. Because of this reason electromagnetic strikes of θ and θ+90^o can not be distinguished using a purely mathematical 2-D model (Swift, 1967; Simpson and Bahr, 2005). In order to overcome this complexity, Swift (1967) suggested skew (conventional skew) parameter and it can be represented as

$$\kappa = \frac{Z_{XX}+Z_{YY}}{Z_{XY}-Z_{YX}} \tag{2.30}$$

This parameter can be used to determine possibility of the two dimensional interpretation. According to Swift (1967), for values of the skew parameter greater than 0.6, which has the meaning for 3D interpretation, the calculated principal directions are meaningless; but for values less than 0.3, which has the meaning for 2D interpretation; the calculated principal directions are accurate to within 10^o (Swift, 1967).

2.2.3 Induction Arrows

Induction arrows (tipper vectors / transfer functions) are vector representations of the complex ratios of vertical to horizontal magnetic field components. Induction arrows can be used to infer the presence or absence of lateral variations in conductivity. Theory of

this method depends on linear combinations of horizontal and vertical magnetic field components (Vozoff, 1991; Simpson and Bahr, 2005).

$$H_z(\omega) = (\mathbf{T}_X(\omega)\ \mathbf{T}_Y(\omega))\begin{pmatrix} H_X(\omega) \\ H_Y(\omega) \end{pmatrix} \tag{2.31}$$

where H_z is vertical magnetic field, H_x and H_Y are horizontal components of the magnetic field and $\mathbf{T}_X$ and $\mathbf{T}_Y$ are complex magnetic field transfer functions generally called the tipper. This method can be used to show which side of a contact is more conductive. That is, near a conductor-resistor boundary, the near surface current density parallel to strike is larger on the conductive side (Vozoff, 1991; Simpson and Bahr, 2005).

These transfer functions (i.e., $\mathbf{T}_X$ and $\mathbf{T}_Y$) are graphically represented by arrows. In the Parkinson convention (Parkinson, 1959), these arrows point toward conductive regions (Vozoff, 1991; Caldwell et al., 2004; Simpson and Bahr, 2005).

On the other hand, in the Wiese convention (Wiese, 1962), these arrows point away from conductive regions. In essence, by the help of induction arrows, the strike can be determined. At the center of the anomaly, the vertical magnetic field decays to zero in the absence of lateral conductivity variations (Vozoff, 1991; Simpson and Bahr, 2005).

2.2.4 The MT Phase Tensor

Caldwell et al., (2004) introduced a method based on treating the phase information as a tensor. The phase tensor method can be useful for determining the geoelectric strike, too. The most striking spot of the phase tensor is that it is not affected by galvanic distortion of the electric field and hence dimensionality of the subsurface may be calculated from distortion-free data. The phase of a complex number (i.e., for this method impedance elements) is defined as the ratio of its imaginary and real parts;

$$\varphi = \frac{Im(Z_{ij})}{Re(Z_{ij})} \tag{2.32}$$

where $\boldsymbol{Z}_{ij}$ denotes elements of the measured impedance tensor and φ is the phase of the impedance tensor elements (Caldwell et al., 2004). As long as the measured (and distorted) impedance is a complex number, it can be written in the form

$$\boldsymbol{Z} = \boldsymbol{X} + \boldsymbol{iY} \tag{2.33}$$

And similarly the regional (distortion-free) impedance can be written as:

$$\boldsymbol{Z}_R = \boldsymbol{X}_R + \boldsymbol{iY}_R \tag{2.34}$$

Also the measured impedance can be written in terms of regional impedance and distortion tensors:

$$\boldsymbol{Z} = \boldsymbol{X} + \boldsymbol{iY} \tag{2.35}$$

$$\boldsymbol{Z} = \boldsymbol{D}(\boldsymbol{X}_R + \boldsymbol{iY}_R) \tag{2.36}$$

$$\boldsymbol{X} = \boldsymbol{DX}_R \tag{2.37}$$

$$\boldsymbol{Y} = \boldsymbol{DY}_R \tag{2.38}$$

Equation of the phase can be written in the tensor form for every elements of the impedance tensor:

$$\boldsymbol{\varphi} = \boldsymbol{X}^{-1}\boldsymbol{Y} = \begin{bmatrix} \varphi_{11} & \varphi_{12} \\ \varphi_{21} & \varphi_{22} \end{bmatrix} \tag{2.39}$$

and similarly the regional (distortion-free) phase can be written as:

$$\boldsymbol{\varphi}_R = \boldsymbol{X_R}^{-1}\boldsymbol{Y_R} \tag{2.40}$$

Furthermore, phase calculated from observed impedance can be written in terms of distortion and regional phase:

$$\boldsymbol{\varphi} = \boldsymbol{D}(\boldsymbol{X_R}^{-1}\boldsymbol{Y_R}) \tag{2.41}$$

The relationship between the phase tensor of the observed and regional impedance tensors can be derived as

$$\boldsymbol{\varphi} = \boldsymbol{D}(\boldsymbol{X_R}^{-1}\boldsymbol{Y_R}) \tag{2.42}$$

$$\boldsymbol{\varphi} = (\boldsymbol{D}\boldsymbol{X_R})^{-1}\boldsymbol{D}\boldsymbol{Y_R} \tag{2.43}$$

$$\boldsymbol{\varphi} = \boldsymbol{X_R}^{-1}\boldsymbol{D}^{-1}\boldsymbol{D}\boldsymbol{Y_R} \tag{2.44}$$

$$\boldsymbol{\varphi} = \boldsymbol{X_R}^{-1}\boldsymbol{Y_R} = \boldsymbol{\varphi_R} \tag{2.45}$$

These formulations prove that the observed and regional phase tensors are independent of the distortion tensor, consistent with the behavior expected for the phase on physical grounds. The phase tensor makes no assumption about the regional dimensionality and is applicable even resistivity structure is 3-D (Caldwell et al., 2004; Bibby et al., 2005).

2.2.4.1 Parameters of phase tensor. All parameters calculated from phase tensor are coordinate invariant but only one of them is coordinate variant (Caldwell et al., 2004). The simplest representations of the invariant parameters are the trace (tr),

$$tr(\varphi) = \varphi_{11} + \varphi_{22} \tag{2.46}$$

the skew (sk) (note that the skew presented here and the skew mentioned earlier under Swift's analysis are two distinct parameters),

$$sk(\varphi) = \varphi_{12} - \varphi_{21} \tag{2.47}$$

and the determinant

$$det(\varphi) = \varphi_{11}\varphi_{22} - \varphi_{12}\varphi_{21} \tag{2.48}$$

of the phase tensor. Also, there are some other parameters which are coordinate invariant

$$\varphi_1 = tr(\varphi)/2 \tag{2.49}$$

$$\varphi_2 = (det(\varphi))^{1/2} \quad (2.50)$$

$$\varphi_3 = sk(\varphi)/2 \quad (2.51)$$

In terms of these quantities the maximum, minimum are given by the expressions:

$$\varphi_{max} = ({\varphi_1}^2 + {\varphi_3}^2)^{1/2} + ({\varphi_1}^2 + {\varphi_3}^2 - {\varphi_2}^2)^{1/2} \quad (2.52)$$

$$\varphi_{min} = ({\varphi_1}^2 + {\varphi_3}^2)^{1/2} - ({\varphi_1}^2 + {\varphi_3}^2 - {\varphi_2}^2)^{1/2} \quad (2.53)$$

There are two parameters, which are very important for graphical representation of the phase tensor, α and β the skew angle given by the expressions

$$\alpha = \frac{1}{2} tan^{-1}\left(\frac{\varphi_{12}+\varphi_{21}}{\varphi_{11}-\varphi_{22}}\right) \quad (2.54)$$

$$\beta = \frac{1}{2} tan^{-1}\left(\frac{\varphi_{12}-\varphi_{21}}{\varphi_{11}+\varphi_{22}}\right) \quad (2.55)$$

where α defines the tensor's dependence on the coordinate system, which is the only coordinate variant parameter, and β can be thought of as a rotation and is a measure of the tensor's asymmetry. Note that β depends on the tensor's skew, which is invariant under rotation but changes sign if the coordinate system is reflected. Also, β takes values between -3 and 3 (Caldwell et al., 2004).

2.2.4.2 Graphical Representation of the Phase Tensor. The MT phase tensor can be graphically represented by an ellipse. In particular, the major and minor axes of the ellipse represent the principal axes and values of the tensor with the orientation of the major axis specified by the angle $\alpha - \beta$. If $\beta = 0$ (symmetric tensor), the orientation of the major axis is given by α. However, in 3-D case, β is different from zero and shows the rotation of the major axis of the phase tensor ellipse away from an identically shaped ellipse represented

by a symmetric tensor. Graphical representation of the phase tensor is shown in Figure 2.1. The direction of the major axis represents the path of electric currents. In other words, the major axis of the phase tensor ellipse shows the geoelectric strike. It is expressed in the previous subject that β is a measure of the tensor's asymmetry. That is, β gives information about the dimensionality of the substructure. For instance, in the 1-D case, β=0 and ellipses are nearly circle (Caldwell et al., 2004).

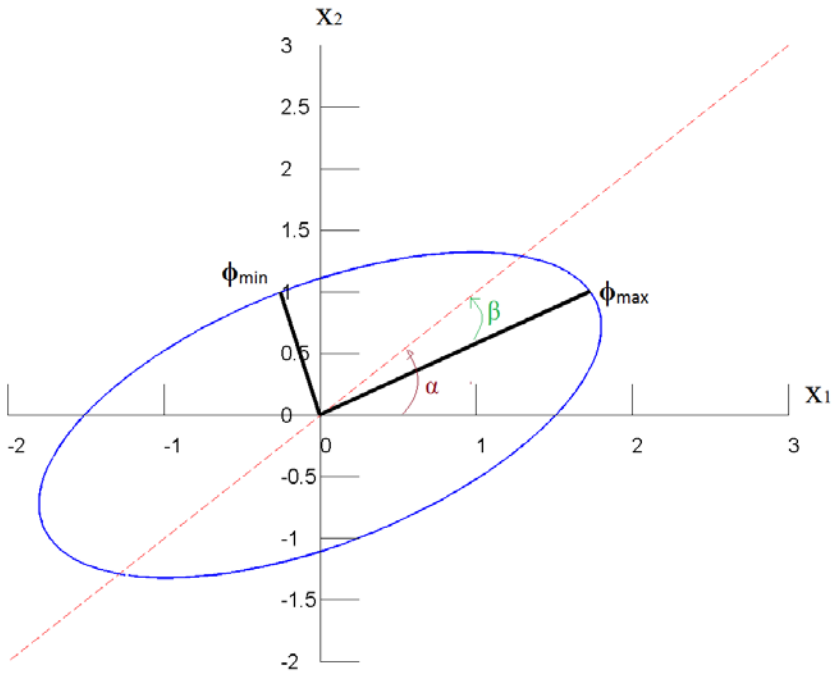

Figure 2.1: Graphical representation of the phase tensor, modified from Caldwell et al., (2004). The major and minor axes of the ellipse are the principal values of the phase tensor. The direction of the major axis of the ellipse, given by the angle $\alpha - \beta$, describes the relationship of the tensor to the observer's reference frame or coordinate system ($x1$, $x2$). If the phase tensor is not symmetric, β is non-zero and it is responsible for determination of the ellipse orientation (Caldwell et al., 2004).

Different visualization tools can be used for representing the phase tensor ellipses. Firstly, normalization of the ellipse axes (major and minor principal values) is an important issue. The most common way of doing so is done by equalizing the major axes of all ellipses. The next step may be painting the ellipses with a color that is to be emphasized (Booker, 2013). For instance, ellipses can be filled with colors that are based on skew angle values and such a figure may be used for determining dimensionality of the media. Moreover, ellipses can be plotted together with induction arrows (Caldwell et al., 2004; Hill et al., 2009; Booker, 2013). In this thesis, induction arrows are concentrated with

ellipses in figures and ellipses are filled with respect to minor axis values, azimuth values, and skew angle.

2.2.4.3 Dimensionality and the Phase Tensor. If the regional conductivity structure is both isotropic and 1-D (i.e. the conductivity varies only with depth), the impedance tensor in a Cartesian coordinate system (x_1, x_2)

$$\mathrm{Z_{1D}} = \begin{bmatrix} 0 & \mathrm{Z_{12}} \\ -\mathrm{Z_{21}} & 0 \end{bmatrix} \tag{2.56}$$

and

$$\Phi = \tan^{-1}(Y_{1D}/X_{1D}) \tag{2.57}$$

then

$$\varphi_{1\mathrm{D}} = \begin{bmatrix} Y_{1D}/X_{1D} & 0 \\ 0 & Y_{1D}/X_{1D} \end{bmatrix} = (Y1\mathrm{D}/X1\mathrm{D})\mathbf{I} = \tan(\varphi)\mathbf{I} \tag{2.58}$$

where **I** is the identity matrix, and **Φ** is characterized by the tangent of the conventional MT phase for a 1-D structure. If the structure is 1-D, the major and minor axis will be the same and phase tensor ellipse turns into a circle (Caldwell et al., 2004).

In 2-D regional structure, in a Cartesian coordinate system (x_1^{I}, x_2^{I}) aligned with x_1^{I} parallel to the (unknown) strike direction, at say an angle θ with respect to the observation coordinate system, the regional impedance tensor $\mathbf{Z_R}$

$$\mathrm{Z'_{R-2D}} = \begin{bmatrix} 0 & \mathrm{Z'_{12}} \\ \mathrm{Z'_{21}} & 0 \end{bmatrix} = \begin{bmatrix} 0 & Z_{||} \\ Z_{\perp} & 0 \end{bmatrix} \tag{2.59}$$

$$\varphi'_{2\mathrm{D}} = \begin{bmatrix} Y_{\perp}/X_{\perp} & 0 \\ 0 & Y_{||}/X_{||} \end{bmatrix} \text{ or } \varphi'_{2\mathrm{D}} = \begin{bmatrix} Y_{||}/X_{||} & 0 \\ 0 & Y_{\perp}/X_{\perp} \end{bmatrix} \tag{2.60}$$

3. DATA

In this chapter, two different forward models will be represented. In addition, details about field data collected around the North Anatolian Fault Zone (NAFZ) near tosya will be represented.

3.1. Homogeneous Half - Space Model

A homogeneous half - space model was constructed with RM3D, a three-dimensional (3D) numerical modeling algorithm developed by Mackie et al. (1993). In the developed model the subsurface of the Earth was taken as 100 Ωm half - space. Figure 3.1a and Figure 3.1b show the response of the homogenous model in TM and TE modes in three frequencies, respectively.

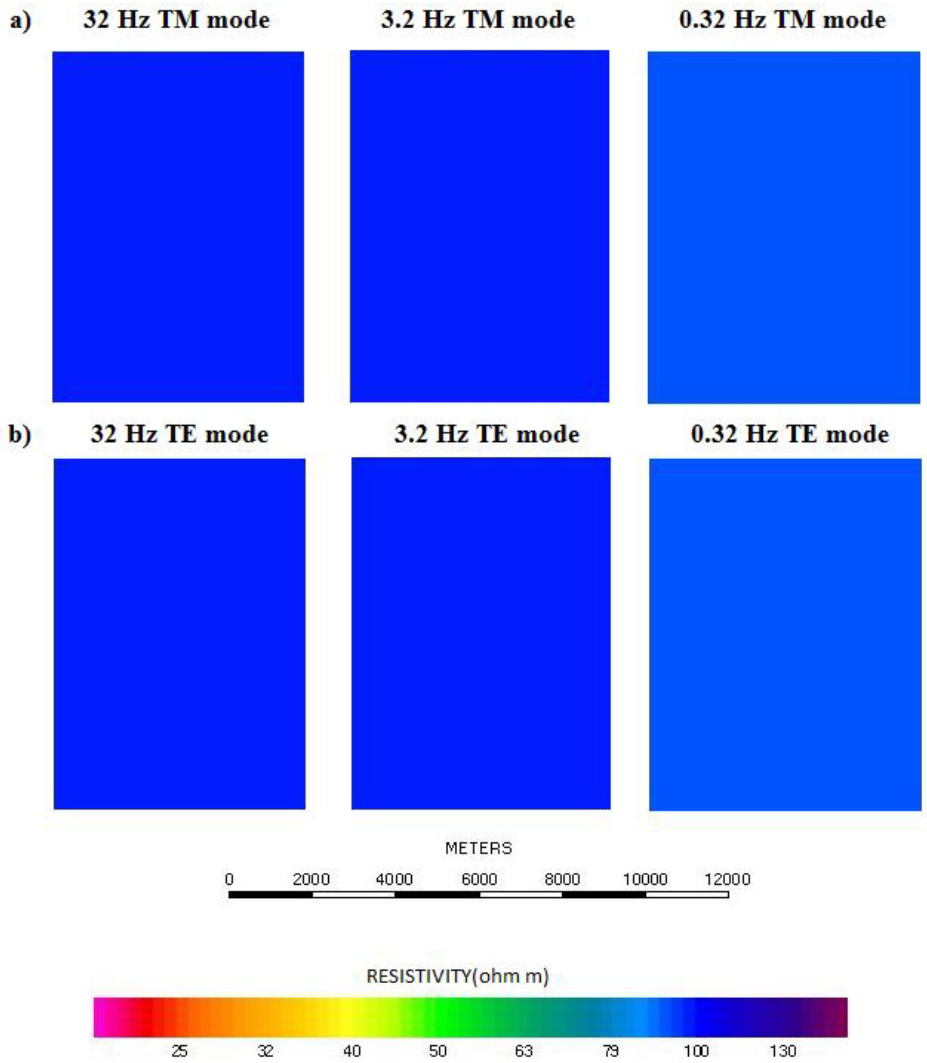

Figure 3.1: a) TE response of the homogeneous forward model. b) TM response of the homogeneous forward model.

Following the construction and calculation of the forward model, a 7 x 7 synthetic MT sounding array was created, i.e. at these synthetic stations the impedance and tipper information were extracted from the model response. The geometry of the sounding locations is shown on Figure 3.2. Then, synthetic data were used as input for the calculation of the MT phase tensor elements and the phase tensor ellipses for this homogeneous model.

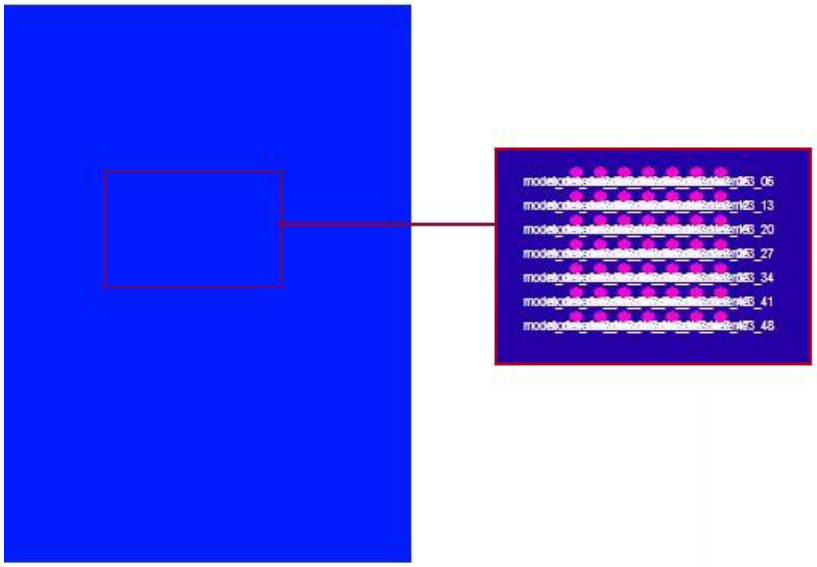

Figure 3.2: Station Locations of the synthetic sounding array. 7 x 7 sounding array was constructed for the homogeneous model.

3.2. Caldwell et al. (2004) Model

Caldwell et al. (2004) have calculated synthetic data with a modeling code described in Xiao (1992) and Xiao & Tripp (1995). In this study, Using RM3D a model that has similar geometry was constructed. Caldwell et al. (2004) model can be described with two conductive features embedded in a 100 Ωm half-space (Figure 3.1). First conductive feature is a small conductive cube (10 Ωm) near the surface and the second feature is a relatively larger conductive rectangular body (1 Ωm) found deeper. Sides of the small cube are 250 m and the distance from surface to its top was 50 m. Deeper conductive body has dimensions of 7 x 3 x 3 km^3 and it is buried 1.5 km below the surface (Figure 3.1).

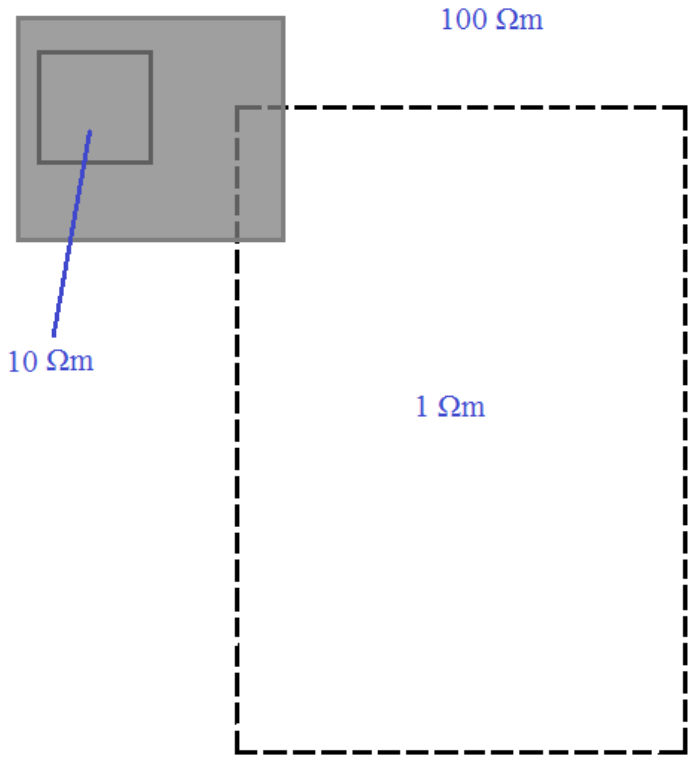

Figure 3.3: Map view of the conductivity model used to illustrate the properties of the phase tensor in a 3-D situation. Grey area shows the region covered by phase tensor ellipses (Caldwell et al., 2004).

A similar procedure used in the construction of a homogeneous half – space case (3.1) was carried on while creating synthetic stations, but this time a 10 x 10 array was formed. This was done for a proper comparison to Caldwell et al. (2004). Synthetic impedance tensor elements were calculated for every station at three different frequencies. These frequencies were 32 Hz (0.0316 sec.), 3.2 Hz (0.0316 sec.) and 0.32 Hz (3.16 sec.) as they appear in Caldwell et al., (2004). The distance between every station is arranged to be 125 m, so the array spans a 1.125 km x 1.125 km area. Map of the array is shown on the Figure 3.5.

On Figure 3.4, approaching form left to right deeper levels of the model could be examined. The upper row demonstrates the TM mode, while the lower row shows TE mode results. The surficial little cube (0.250 km^3) that was buried to a depth of 50 m appeared on both of the modes at 32 Hz. Effects caused by both the small and the deep conductors became clearer at the 3.2 Hz figure. Likewise, the large rectangular shaped conductor (7 x 3 x 3 km^3) that was placed at 1.5 km depth dominated the model response on both TM and TE modes.

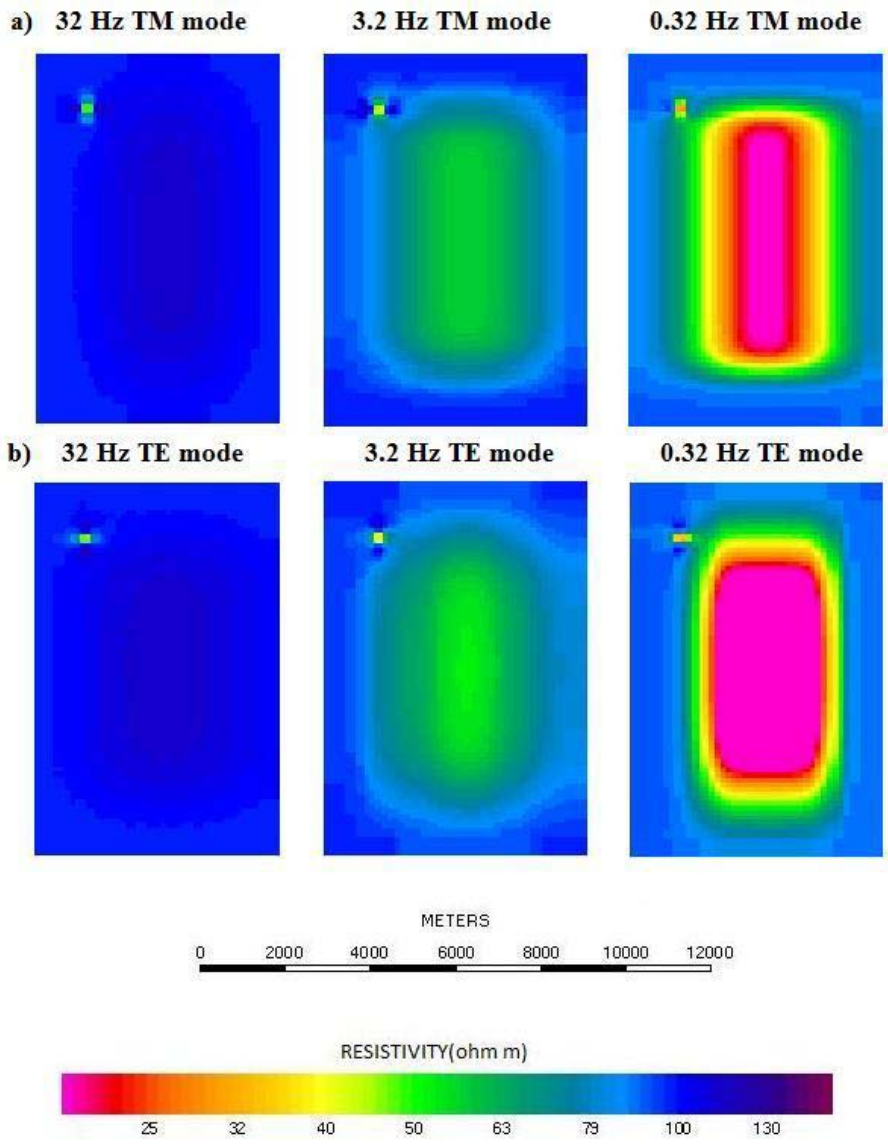

Figure 3.4.: Responses of the 3D forward model. a) TE Mode Response of the calculated model. Model response for 32 Hz. As long as higher frequencies include information from shallow parts, in this figure the cube with 10 Ωm resistivity occurs. Model response for 3.2 Hz. Middle frequencies include information from middle depth parts, in this figure the cube with 10 Ωm resistivity and the rectangular shaped conductor (1 Ωm) occurs. Model response for 32 Hz. Low frequencies include information from shallow parts, in this figure the rectangular shaped conductor (1 Ωm) is dominated the model response as it can be seen. b) TM Mode Response of the calculated model.

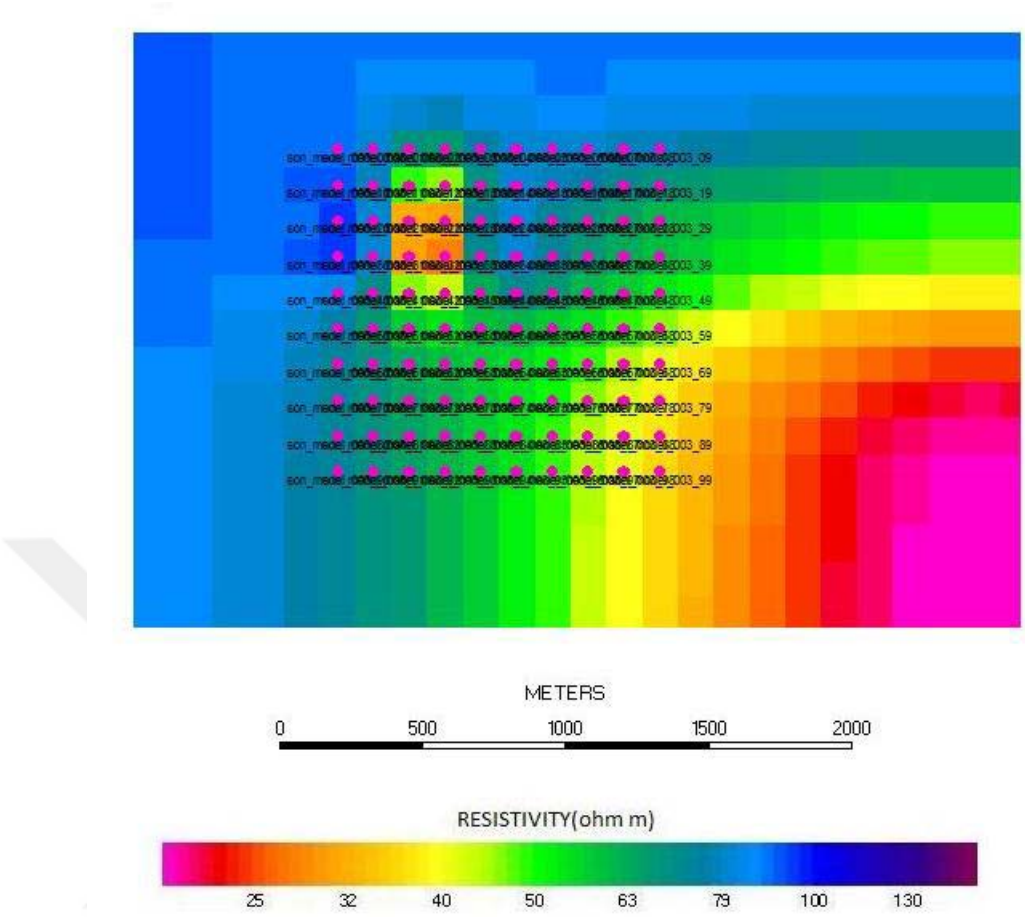

Figure 3.5. Station Locations of the synthetic sounding array. The distance between every station is 125 m. Stations have been located between the cube and rectangular shaped conductor so as to see the directions and shapes of the ellipses and induction vectors as it has done in Caldwell et al., (2004).

3.3. Case study

A third test on the MATLAB® scripts developed in this thesis was performed by applying them on field (observed) data and checking the phase tensor values. For this purpose phase tensors were calculated and figures were drawn as map-views for different frequencies as well as phase tensor pseudo-sections made up of 40 frequencies available at every observation point along a two-dimensional profile.

Study area chosen for the phase tensor analysis is located at the south of Black Sea within Central Pontides (Okay and Tüysüz et al., 1999, Okay et al., 2013). Central Pontides are made up of two major tectonic entities. These are the İstanbul Zone and the Sakarya Zone (Okay and Tüysüz et al., 1999, Okay et al., 2013, Aygül et al., 2015). The tectonic evolution of the study area can be explained by northward motion of the Anatolid-Tauride Block during closure of the Tethys Ocean. The Anatolide-Tauride Block subducted under the Sakarya Zone. After this event accretionary units emplaced on the Anatolid-Tauride Block (Okay and Tüysüz, 1999; Espurt et al., 2014).

Phase tensor ellipses were plotted by using data collected at 25 wide-band (320 Hz – 1800 sec.) MT stations that form a north – south aligned profile crossing the central North Anatolian Fault Zone (NAFZ) near Tosya, Kastamonu as well as the İzmir-Eskişehir-Ankara-Erzincan (IEAE) Suture. The profile went across Domuzdağ and Çangaldağ Massifs as part of the Central Pontide Supercomplex (CPS), an east – northeast aligned metamorphic belt (Okay et al., 2013; Aygül et al., 2015) positioned at the north of NAFZ. At the south, however, the profile went across Orta-Devrez Fault and Kızılırmak Fault Zones (Yolsal- Çevikbilen et al., 2012) as well. Along with the massifs found at the north of the NAFZ, subduction related accretionary units define the area whereas at the south ophiolites are more abundant (Aygül et al., 2015).

Black dots on Figure 3.6 represent the MT observation positions where site separation along the profile was taken as 3 - 5 km on average, except the vicinity of the NAFZ. Near NAFZ site separation was much denser (~ 1 km) for getting higher resolution around the fault.

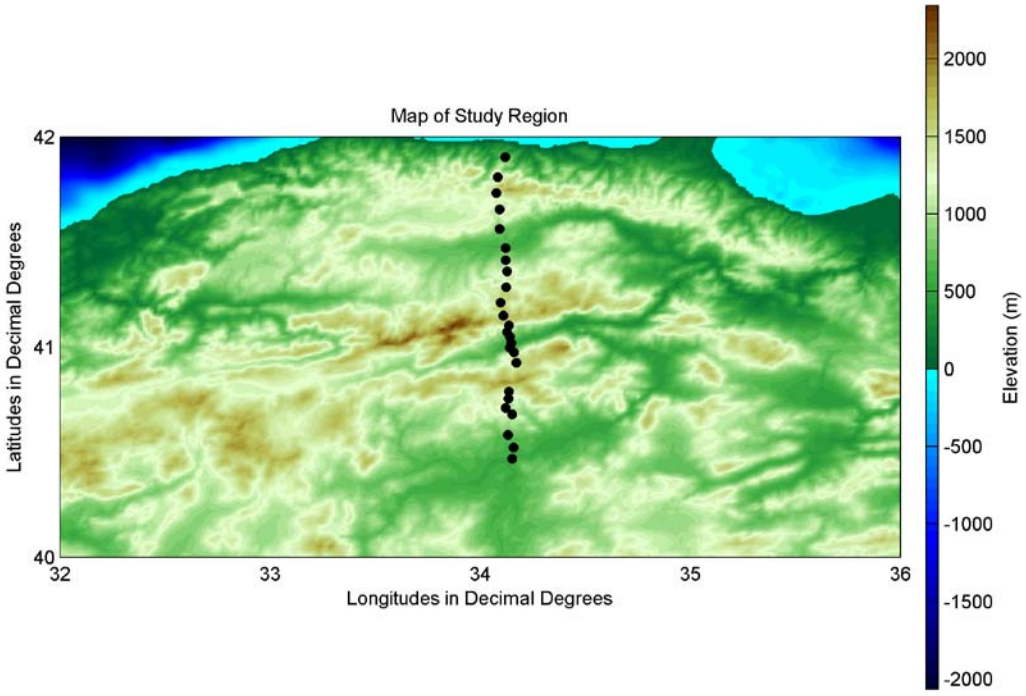

Figure 3.6: Map of study region. Black dots show measurement site locations.

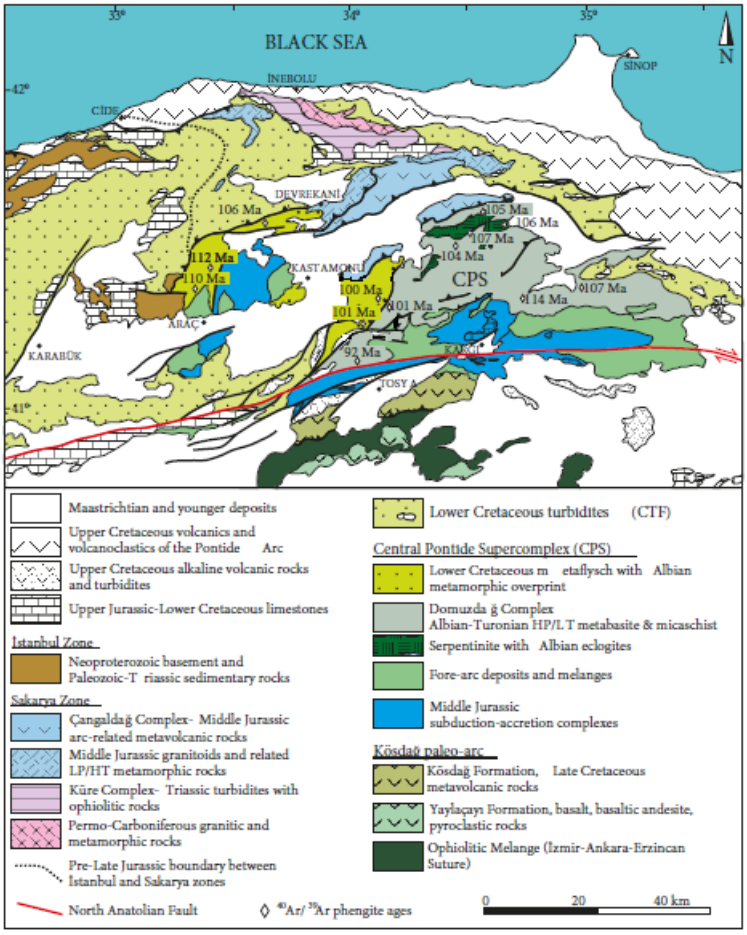

Figure 3.7: Tectonic map of Central Pontides modified from Aygül et al. (2015)

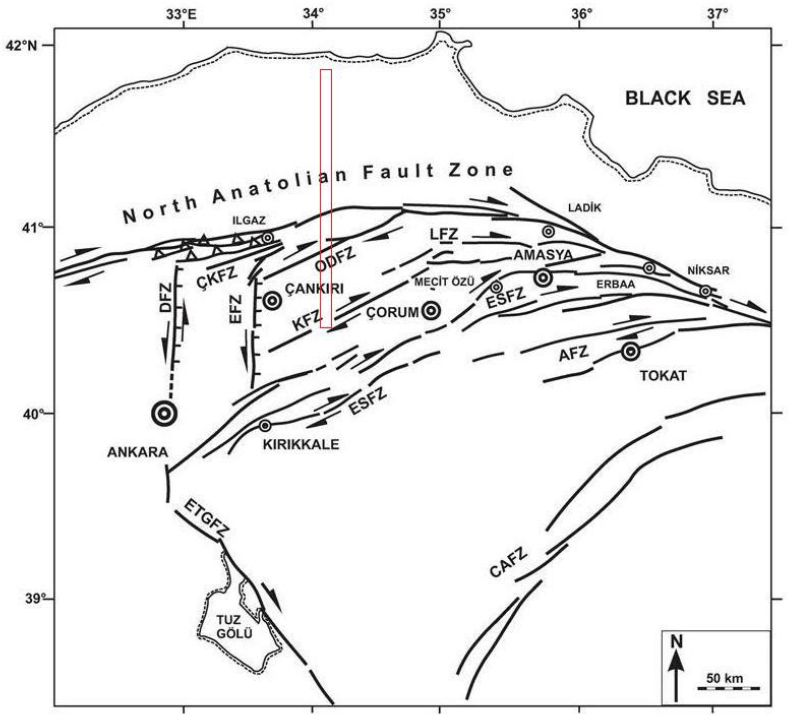

Figure 3.8: Simple fault map of the study area rearranged from Yolsal-Çevikbilen et al., (2012). Red rectangle represents location of the MT profile. AFZ: Almus Fault Zone, CAFZ: Central Anatolian Fault Zone, ÇKFZ: Çerkeş-Kurşunlu Fault Zone, DFZ: Dodurga Fault Zone, EFZ: Eldivan Fault Zone, ESFZ: Ezinepazarı-Sungurlu Fault Zone, ETGFZ: Eskişehir- Tuzgölü Fault Zone, KFZ: Kızılırmak Fault Zone, LFZ: Laçin Fault Zone, ODFZ: Orta-Devrez Fault Zone (Yolsal- Çevikbilen et al., 2012).

4. RESULTS

4.1. Homogeneous Half-Space Model Results

In order to test the validity of the MATLAB® scripts, a comparison was realized by using homogeneous half - space model. The phase tensor ellipses should have circular shapes if MATLAB® scripts for phase tensor method are functioning correctly. Results of this test are shown on Figure 4.1. At every frequency, ellipses appeared circular shaped as expected (Figure 4.1). The skew values came out around zero as well (Figure 4.1). This homogeneous half - space test implied that the phase tensor MATLAB® scripts were ready for comparison with Caldwell et al. (2004) results.

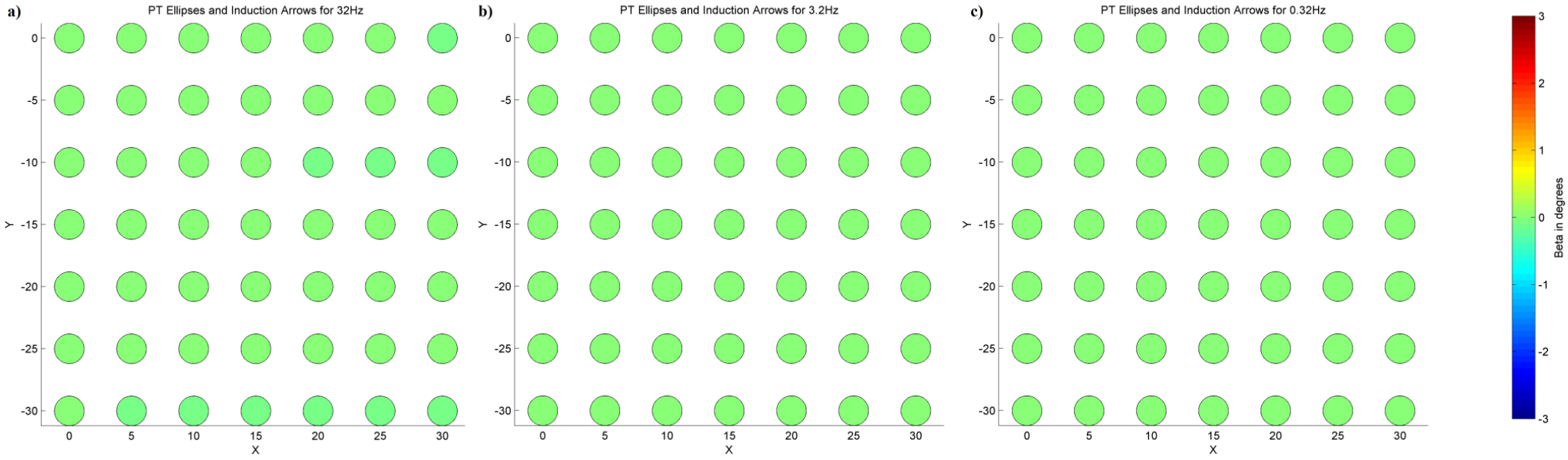

Figure 4.1: Map of phase tensor ellipses at three different frequencies [a)32hz b)3.2hz c)0.32hz] for the model shown in Figure 3.1. In 1D, homogeneous media, ellipses turn into circles.

4.2 Results of Caldwell et al., (2004)

Figure 4.2 and Figure 4.3 summarize the map views of the phase tensor ellipses drawn originally by Caldwell et al. (2004) at three distinct periods (0.0316 sec., 0.316 sec. and 3.16 sec., respectively). These two figures include identical phase tensor ellipses with identical structure, but the contours and the grey tone fillings vary between the two figures. On Figure 4.2 the ellipses were painted with the azimuth of major axis, whereas the ellipses on Figure 4.3 were painted with the skew angle. Induction arrows are graphical representation of real parts of tipper vectors (Parkinson, 1959). In addition, Figure 4.2 involves induction arrows in Parkinson convention (that is, induction arrows are pointing to the higher conductivity; see Parkinson (1959) for more details) for comparison. The bold black line represents the borders of the surficial cube (half of it) with 10 Ωm that was described on Figure 3.3. Likewise dashed line represents the corner of the deep rectangular prism with 1 Ωm, again described in the model on Figure 3.3.

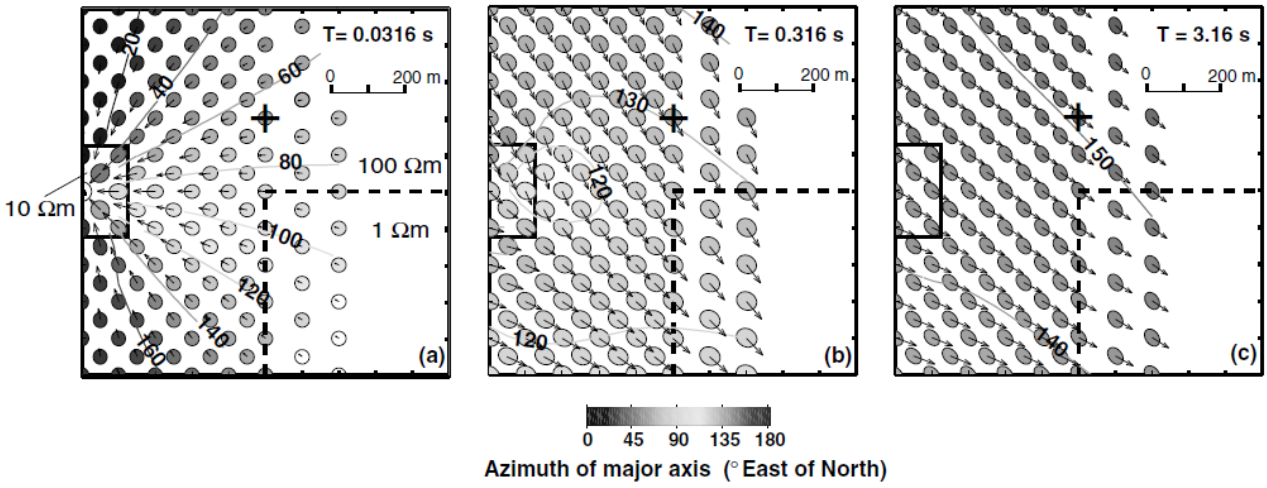

Figure 4.2: Maps of the phase tensor ellipses and induction arrows (real part) at three different periods for the model shown in Figure 3.1. Contours and grey tone fillings correspond to the azimuth of the major axes of ellipses.

It is quite clear that at short periods (namely 0.0316 sec.) on Figure 4.2, deep conductor did not have any influence on the MT responses and ellipses have radial

alignment around the cube. Alignment would be tangential if the structure was appointed as resistive. The change in alignment in that way suggests that the direction of the major axes indicates preferred flow direction of the induced current.

At the shortest period (0.0316 sec.), induction arrows and the contour lines of the major axes of the phase tensor ellipses are almost parallel. At intermediate period (0.316 sec.), however the major axes alignments show a mixture of the effects of both the shallow (10 Ωm) and deep (1 Ωm) conductors. At the longest period (3.16 sec.), inductive effects from cube disappear and the deep conductor dominates the phase tensor response. The major axes alignments show the preferred flow direction of the induced current relevant to the deep conductor.

On Figure 4.3 phase tensor ellipses painted with skew angle (β) values are shown. At the shortest period (0.0316 sec.), the skew angle is zero around at the axes of symmetry and takes highest values around corners of the conductive cube. It takes highest values around the corners of the cube because of the asymmetrical conductivity distribution at the measurement point. At the intermediate period (0.316 sec.), changes in the skew angle values are more complicated because of the effects of two conductive bodies. At the longest period (3.16 sec.), the skew angle reflects only the effect of deep conductor.

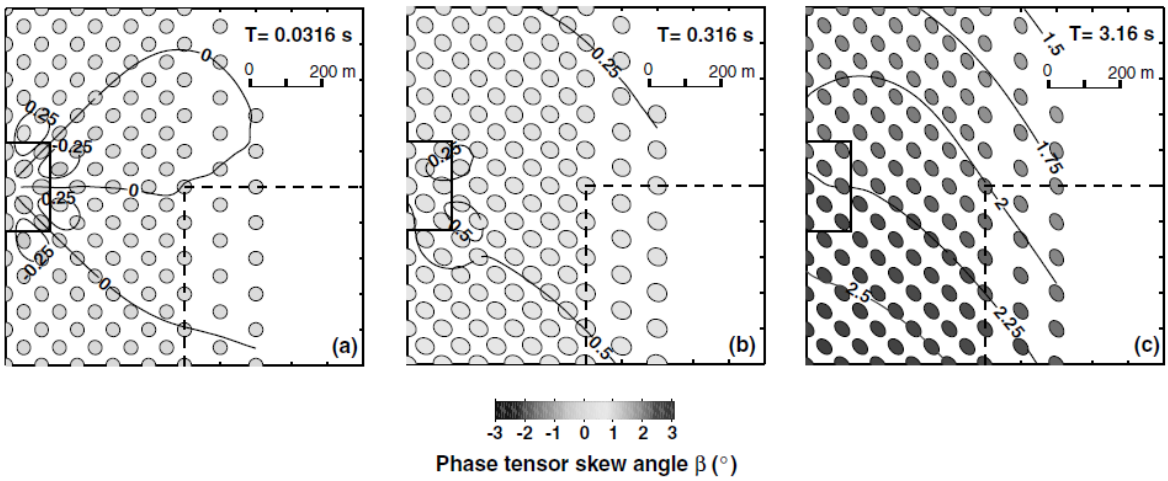

Figure 4.3: Maps of phase tensor ellipses and induction arrows (real part) at three different periods for the model shown in Figure 3.1. Contours and grey tone fillings correspond to skew angle.

4.3 Results of This Study

On Figure 4.4 phase tensor ellipses were shown with induction arrows and painted in color with azimuth of the major axes values. At the shortest period (0.032 sec.), the phase tensor map of Caldwell et al., (2004) (Figure 4.2) and result of this study (Figure 4.4) are almost identical. That is, the major axis alignments are in the direction of preferred induced current flow and ellipses have radial alignment around the conductive cube. Likewise, induction arrows point to the surficial conductive cube. At the intermediate period (0.316 sec.) on Figure 4.3 and Figure 4.4, the major axes alignments represent mixture of the shallow conductive cube and the deep rectangular shaped conductor. Induction arrows are also affected from these conductors at the intermediate period figure. There are some differences at some of the phase tensor ellipses on Caldwell et al. (2004) (Figure 4.3) and this study (Figure 4.4). Presumably, the difference between Caldwell et al. (2014) results and this studies result may be due to the use of different modeling algorithm and mesh**.** At the longest period (320 sec.), the ellipses do not show any direction. Normally, their major axes must show the direction of preferred flow or the location of the deep conductor as it is in Caldwell et al. (2004). Again that difference may be caused

because of the forward modeling codes or meshes. A similar problem can be seen on the induction arrow plots.

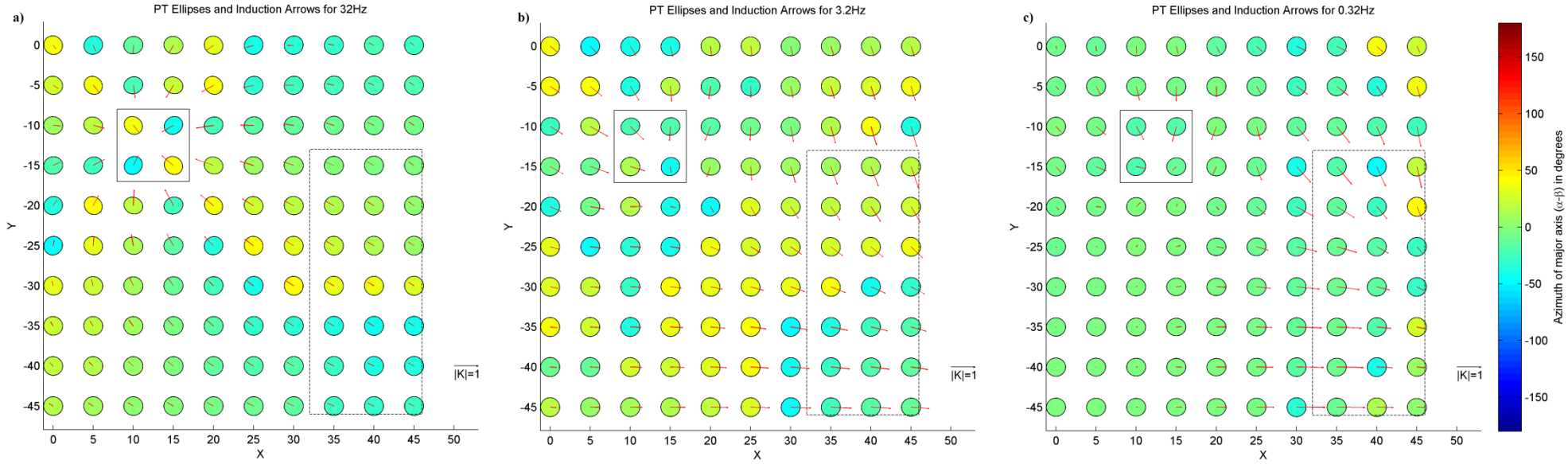

Figure 4.4: Map of phase tensor ellipses and induction arrows (real part) at three different frequencies for the model shown in Figure 3.3. Fillings correspond to the azimuth of major axes of ellipses.

On Figure 4.5 phase tensor ellipses painted in color with skew angle values were shown. At the shortest period, the skew angle values are nearly zero at the axes of symmetry and takes greater values around corners and outside of the conductive cube. That is because of the asymmetrical conductivity distribution. At the intermediate period, on Figure 4.5, changes in the skew angle values were more complicated because of the effects of two conductive bodies. At the lowest frequency, on Figure 4.5, the skew angle reflects only the effect of deep conductor. From the skew angle point of view, all these results were similar when compared with the results of Caldwell et al., (2004).

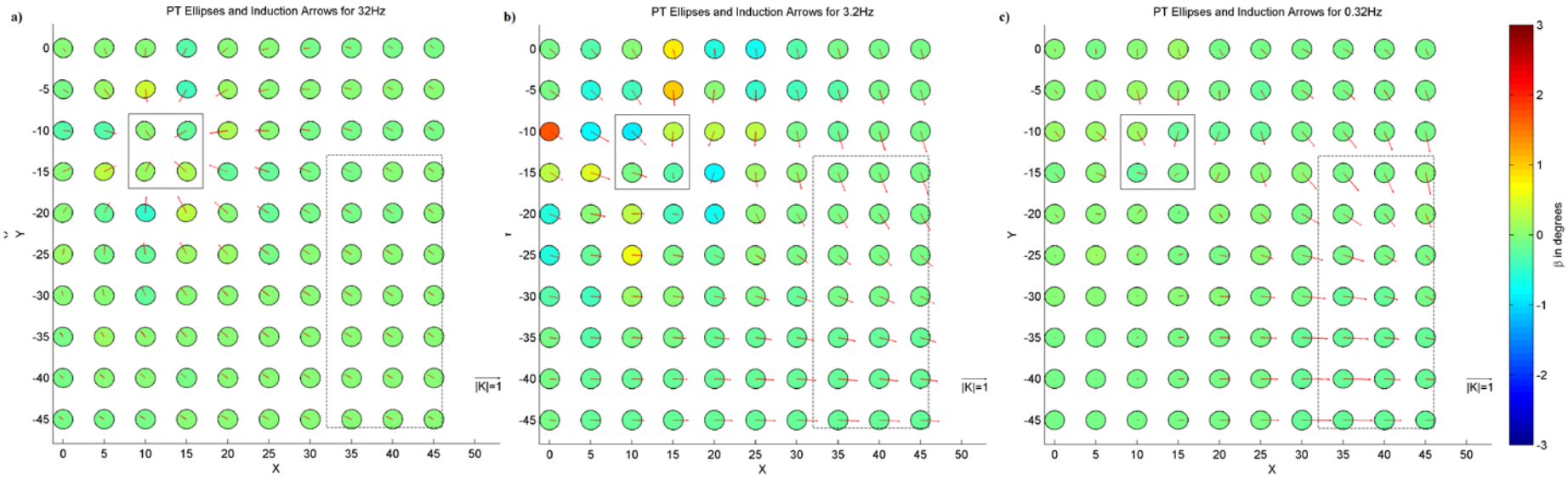

Figure 4.5: Map of phase tensor ellipses and induction arrows (real part) at three different frequencies for the model shown in Figure 3.3. Fillings correspond to the skew angle (β) values of ellipses.

4.4. Other Field Examples

In the original study of Caldwell et al. (2004), the authors analyzed MT data collected at the Taupo Volcanic Zone (TVZ) on the north island of New Zealand. They claimed that the central part of the TVZ could be identified by an area of low gravity where volcano-clastic sediments appeared as conductive compared to the underlying basement rocks (Caldwell et al., 2004). According to Caldwell et al., (2004) the major axes of the phase tensor ellipses near this margin were oriented parallel and perpendicular to the strike of the gravity gradient. They added that in a 2-D conductivity distribution, the induction arrows would be perpendicular to the strike of the conductivity distribution. They pointed out that the agreement between the directions of the induction arrows and ellipse axes near the southeastern margin of the TVZ is good (Caldwell et al., 2004).

Similarly, as an extension to Caldwell et al., (2004), Heise et al., (2007) used the MT phase tensors to represent deep conductor beneath the TVZ. The orientation of the ellipse axes indicated the direction of the conductivity gradient in the deeper range determined by the longer periods. According to Heise et al., (2007), phases greater than 45^{o} indicated increasing conductivity. At southeastern (SE) margin of the TVZ, the phase-tensor ellipses changed their orientation by 90^{o}. At the centre of the TVZ, phase values reached to a peak at periods of nearly 30 sec. indicating that the lower crust is conductive beneath this region (Heise et al., 2007).

As a third example, Hill et al. (2009) used the phase tensor information to investigate distribution of melt beneath Mount St. Helens and Mount Adams. These volcanoes belong to Cascade mountain range and located on the margins of a mid-crustal zone of high electrical conductivity. With the MT method, Hill et al. (2009) found a localized zone of high conductivity beneath Mount St. Helens that extends downward to join the mid-crustal conductor. Moreover, they inferred that the conductivity anomaly associated with the localized zone is caused by the presence of partial melt (Hill et al., 2009).

4.5. Case Study Results

In this study observed MT data from central part of the North Anatolian Fault Zone (NAFZ) were analyzed with phase tensors. The NAFZ is one of the most active fault zones on Earth (Barka, 1992). It extends from Karlıova, in eastern of Turkey, to the Gulf of Saros in Aegean Sea. It is seismically active right lateral strike slip fault and has a length of approximately 1500 km (Barka, 1992; Yolsal-Çevikbilen et al., 2012). Active tectonics of the NAFZ can be explained by complex collision of the Arabian, African and Eurasian plates and resulting westward extrusion of Anatolian plate between right lateral NAFZ and left lateral EAFZ (Yolsal-Çevikbilen et al., 2012).

Phase tensor ellipses and induction arrows were superimposed on topography map of the region for three periods, i.e., T=0.1, 1.33 and 113.6 s, as shown on Figure 4.6. The phase tensor ellipses on this figure have parallel alignment on the NAFZ. On Figure 4.7, ellipses were painted with skew values to have an idea about dimensionality of the subsurface. At every period skew values changed but at short and intermediate periods most ellipses took skew values around zero. At the long period (113.6 sec.), however, a significant skew value changes could be seen. At intermediate (1.33 sec.) and long (113.6 sec.) periods, some ellipses were not drawn since their skew values were out of the acceptable skew value range (for this survey the acceptable range of skew values is $-10^{o} < \beta < 10^{o}$). On such cases, only induction arrows were allowed to represent the observation stations. On both figures, the phase tensor ellipses had the highest rotation at the vicinity of the fault zones. For instance, the phase tensor ellipses had almost parallel alignment to the trend of NAFZ. Getting further away from the fault zones ellipses had different alignments.

On Figure 4.8, we divided the study area into three distinct areas by examining the phase tensor ellipses and the induction arrows. At Zone I, the phase tensor ellipses of the second station at short period showed nearly east-west alignment. On the other hand, at intermediate and long periods, ellipse azimuths change and the major axes of the ellipses show nearly northwest-southeast alignment. The second station of the profile is located around three different geological formations; Cretaceous –Eocene volcano-sedimentary sequence of the Black Sea Margin, Lower Cretaceous siliciclastic turbidites and Küre

complex (Okay et al.; 2006). Existence of these formations and boundaries of them may urge the ellipses to align in the same direction with one of these geological structures. At zone 1, another important geological structure that affects ellipse alignments is Ekinveren fault. Ekinveren fault is a boundary between Eocene & more younger rocks and Permo-Triassic methabasite phyllite (Çangaldağ and Kargı Complexes) (Okay et al., 2006). Station 4 is the nearest station to Ekinveren Fault. At all periods of the fourth station, the major axes alignments of the phase tensor ellipses show some direction. Especially at long period, alignment of the ellipse major axis is nearly north-south. When boundary nature of Ekinveren fault is taken into account, alignment of the major axis may be caused by Ekinveren fault.

At Zone II, effects of the NAFZ on the phase tensor ellipses can also be seen. The phase tensor ellipses and induction arrows of all stations were in good agreement to show the NAFZ. At the fault zone ellipse azimuths are nearly parallel to NAFZ. Induction arrows at this zone's stations tend to point at each other. That gives an idea about a large zone between poor and good conductors. These two techniques support each other very well.

At Zone III, southernmost station of the profile was the one nearest to the Kızılırmak Fault Zone (KFZ). Effects of this fault on the phase tensor ellipses are minor. That is, the major axes of the ellipses appoint Kızılırmak Fault Zone. Effect of KFZ on induction arrows gets visible at some depth. At the longest period (113.6 sec.), phase tensor ellipses and induction arrows support each other. Induction arrows of the southernmost two stations point at each other, indicating a boundary between them.

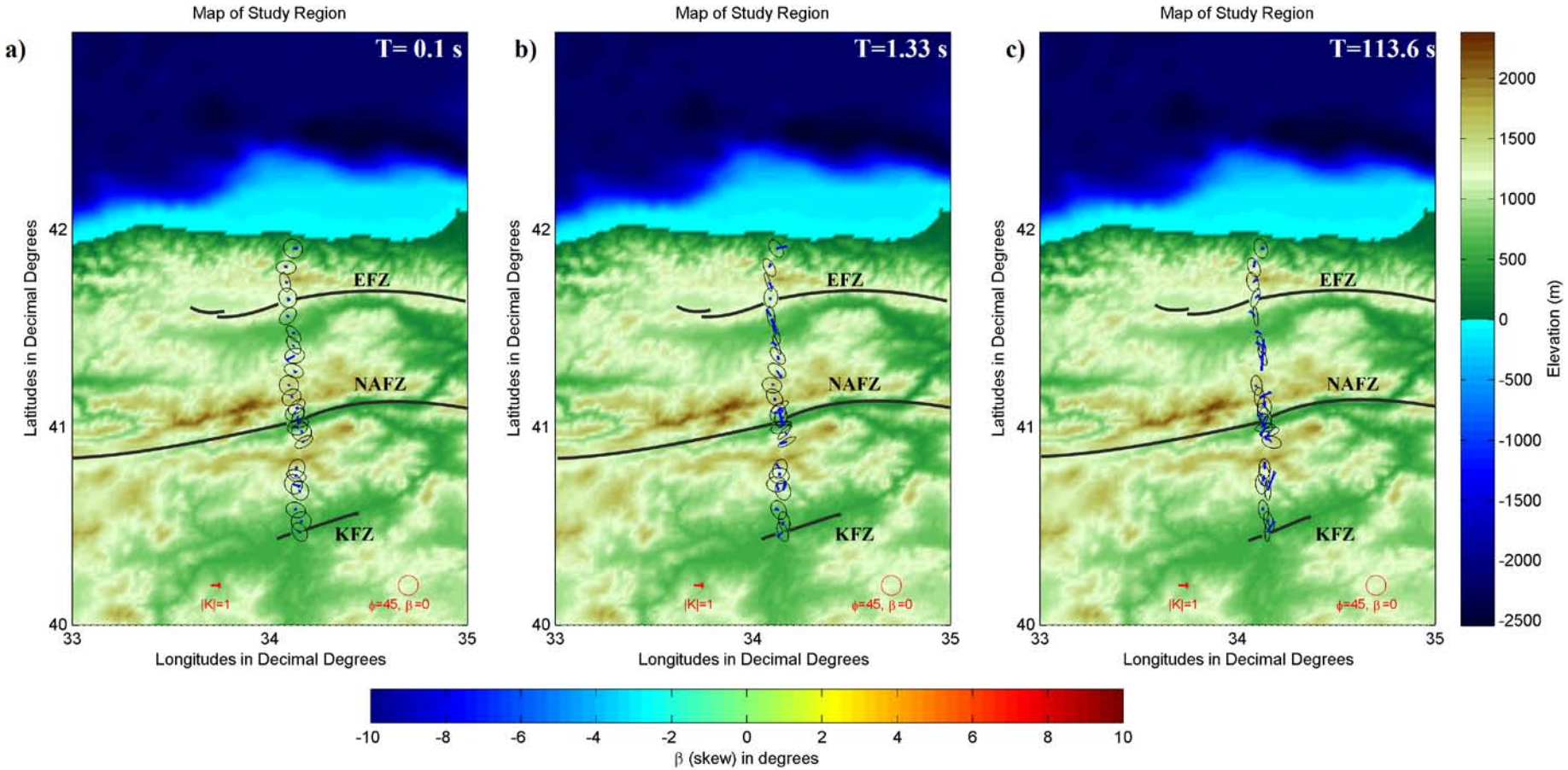

Figure 4.6: Phase tensor ellipses and induction arrows superimposed on topography map at three periods. a) responses at T=0.1 s b) responses at T=1.33 s c) responses at T=113.6 s. Red drawings are legends for induction arrows and unit circle for phase tensor ellipses. Bold curves are representative fault zones in map (EFZ: Ekinveren fault zone, NAFZ: North Anatolian Fault Zone, KFZ: Kızılırmak Fault Zone)

Phase tensor ellipses were drawn as (a north-south profile) pseudo-sections for all available periods as shown on Figure 4.9. On Figure 4.9 ellipses were painted with the minimum phase values. It is pointed out by Heise et al. (2007) and Booker, (2013) that the value of the minimum phase indicates a change in the conductivity (with depth). Minimum phases greater than 45^{o} indicate increasing conductivity. Figure 4.10 is an interpreted version of Figure 4.9. On Figure 4.10, blue rectangles on the pseudo-sections correspond to known geological structures. The first blue rectangle area (at the fourth station) may coincide with Ekinveren Fault Zone (EFZ). As long as EFZ behaved as a transition boundary between Eocene/younger aged rocks at north and Kargı massif at the south, shapes and directions of the phase tensor ellipses were satisfactory when taking this property of the EFZ. The second window on the figure corresponds to NAFZ. At some depth, the major axes of the phase tensor ellipses have nearly east-west alignment. That may be an indication of the main and/or some branches of the NAFZ. The southernmost blue rectangle corresponds to Kızılırmak Fault Zone. The last station of the profile is the nearest station to KFZ. The phase tensor ellipses again showed a boundary. At the northernmost and southernmost blue rectangles, ellipses showed faults but at the intermediate rectangle ellipses align nearly parallel to NAFZ direction. The reason of that situation may be explained in three steps;

- At the northernmost rectangle, the fourth station from the north is near Ekinveren Fault Zone and the major axes of the phase tensor ellipses showed flow of the electrical field. That is, electrical field travels toward EFZ.

- At the middle rectangle, measurements were performed as close as possible on and around the NAFZ. This measurement method caused a high resolution around the study area. Because of the fact that NAFZ is the most important fault on the profile, this measurement method had been used. Some ellipses (station no.13 to 17) had an alignment nearly parallel to the NAFZ and some ellipses (station no. 12 and 18) have the alignment perpendicular to the NAFZ. Ellipses that have perpendicular alignment to the NAFZ are the starting and ending points of the fault zone. That is, station 12 and 18 are the starting and ending points of the fault zone, respectively, and the major axes of the ellipses point towards fault zone.

Moreover, stations between station 13 and station 17 are in the fault zone. Ellipse major axes of that station range had parallel alignment to the NAFZ.

- At the southernmost rectangle, the southernmost station is near Kızılırmak Fault Zone and the major axes of the phase tensor ellipses showed flow of the electrical field. That is, electrical field traveled towards to KFZ.

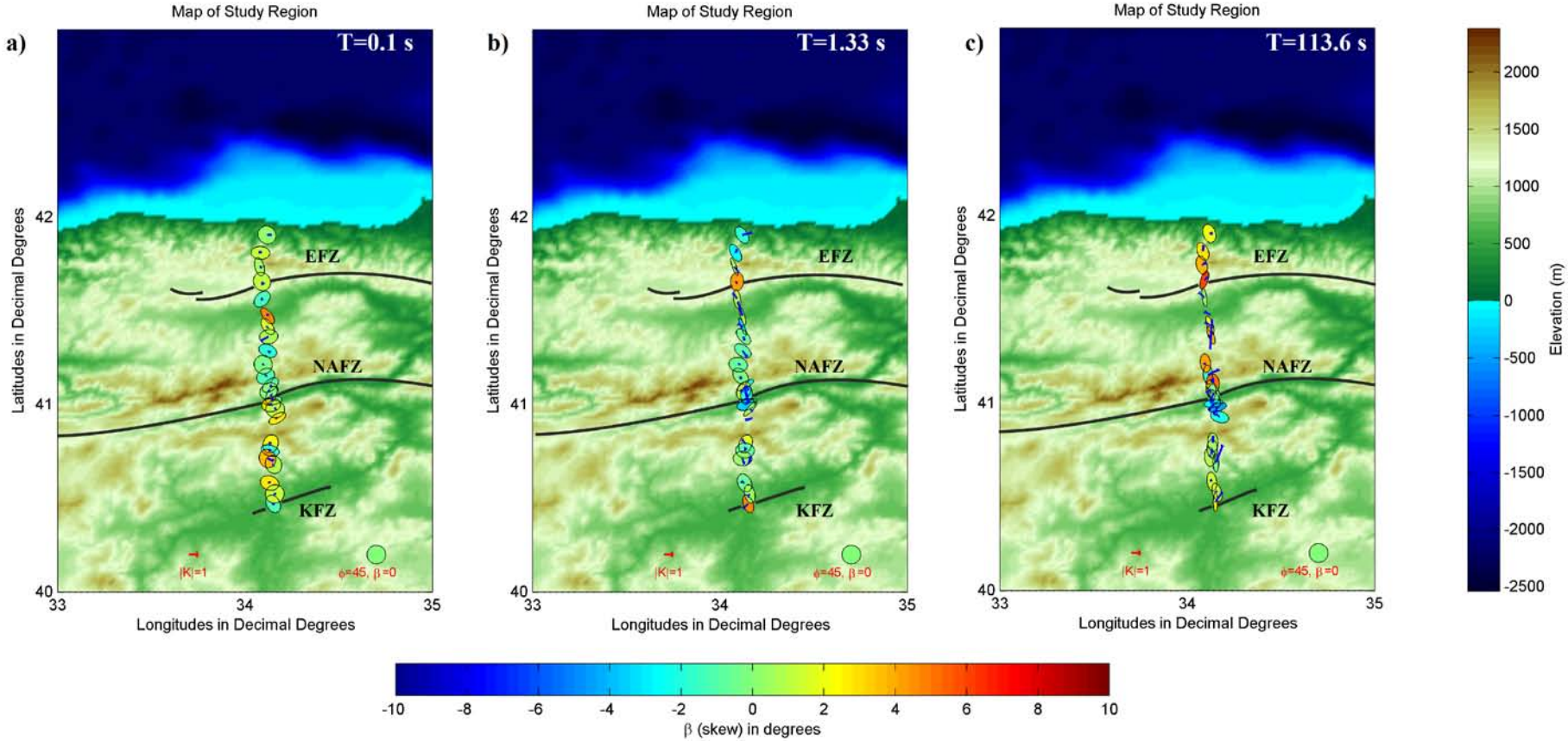

Figure 4.7: Phase tensor ellipses filled with skew values. That's the same of the previous figure. Only ellipses filled with skew values. Bold curves are representative fault zones in map (EFZ: Ekinveren fault zone, NAFZ: North Anatolian Fault Zone, KFZ: Kızılırmak Fault Zone).

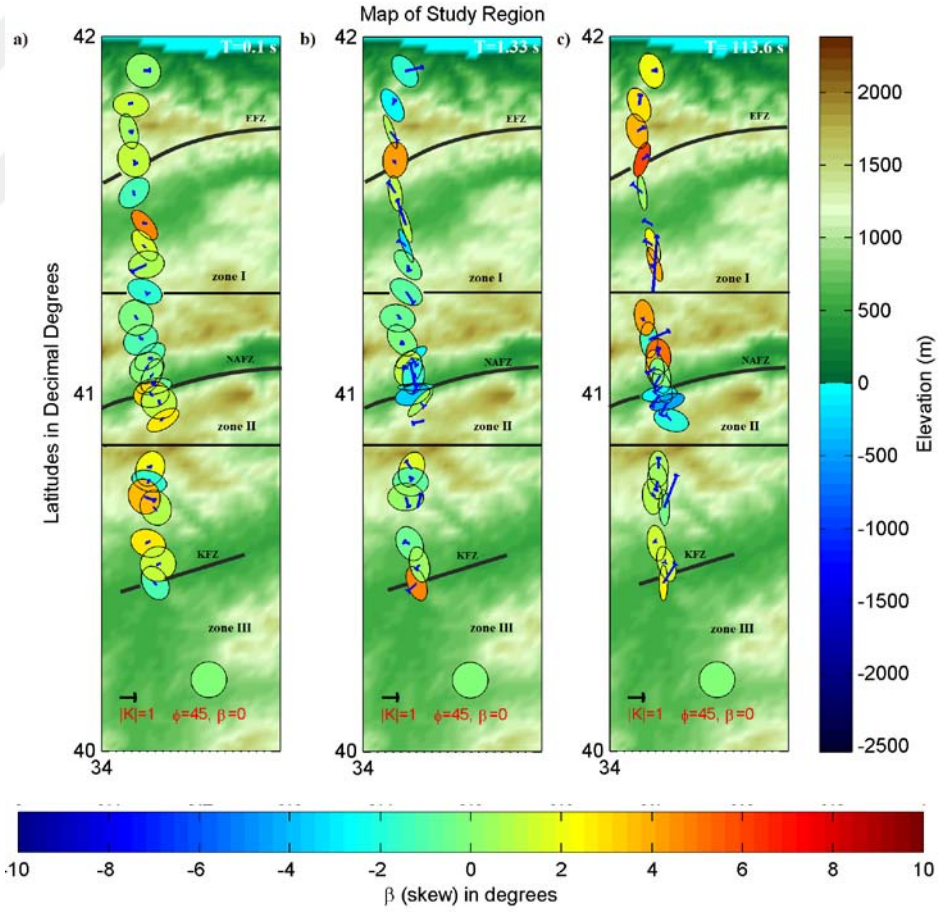

Figure 4.8: In order to make clear interpretations, study area is divided into 3 zones. That is the zoomed version of the Figure 4.7. Bold curves are representative fault zones (EFZ: Ekinveren fault zone, NAFZ: North Anatolian Fault Zone, KFZ: Kızılırmak Fault Zone).

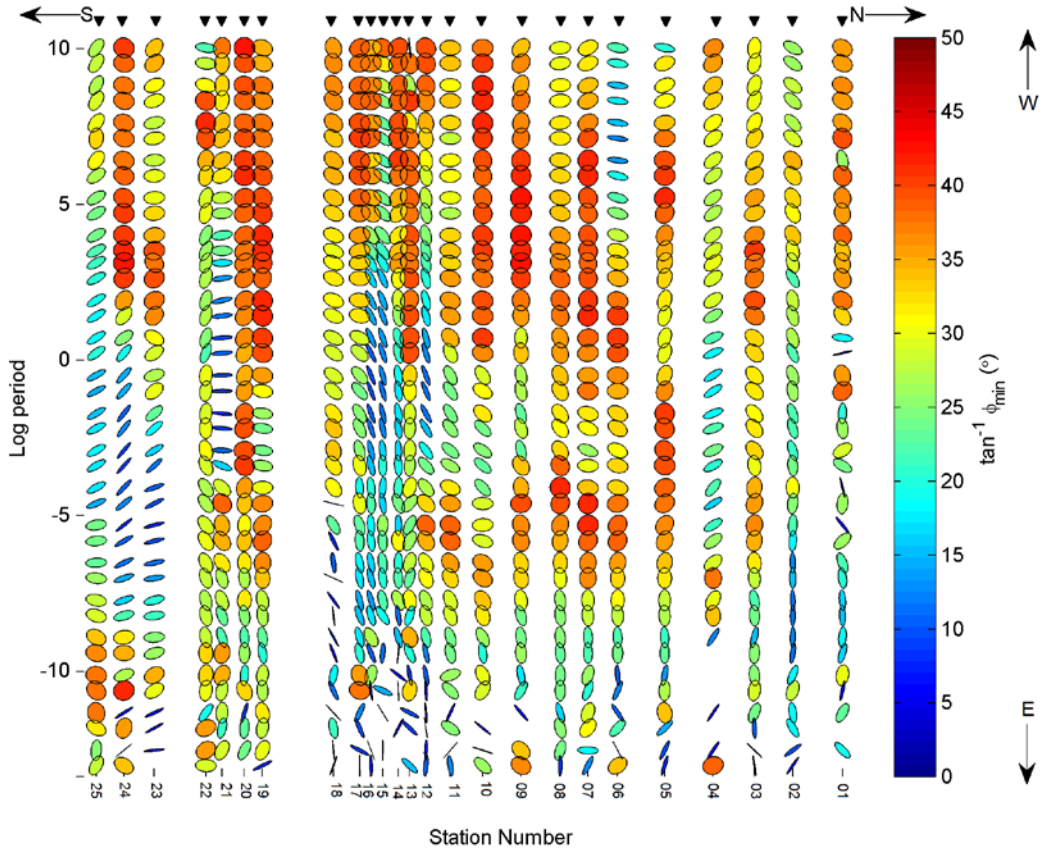

Figure 4.9: Pseudo-section of the phase tensor ellipses. Ellipses are shown in bird's-eye view. MT Profile Alignment is in the N-S direction and the first station is placed at north (the first one is at right). Ellipses are drawn at all periods (major axis directions are in the same direction with geographical N-S-E-W). Some of ellipses were not drawn because their minimum phase colors did not take place in the range shown by color legend. Black triangles represent MT sounding locations.

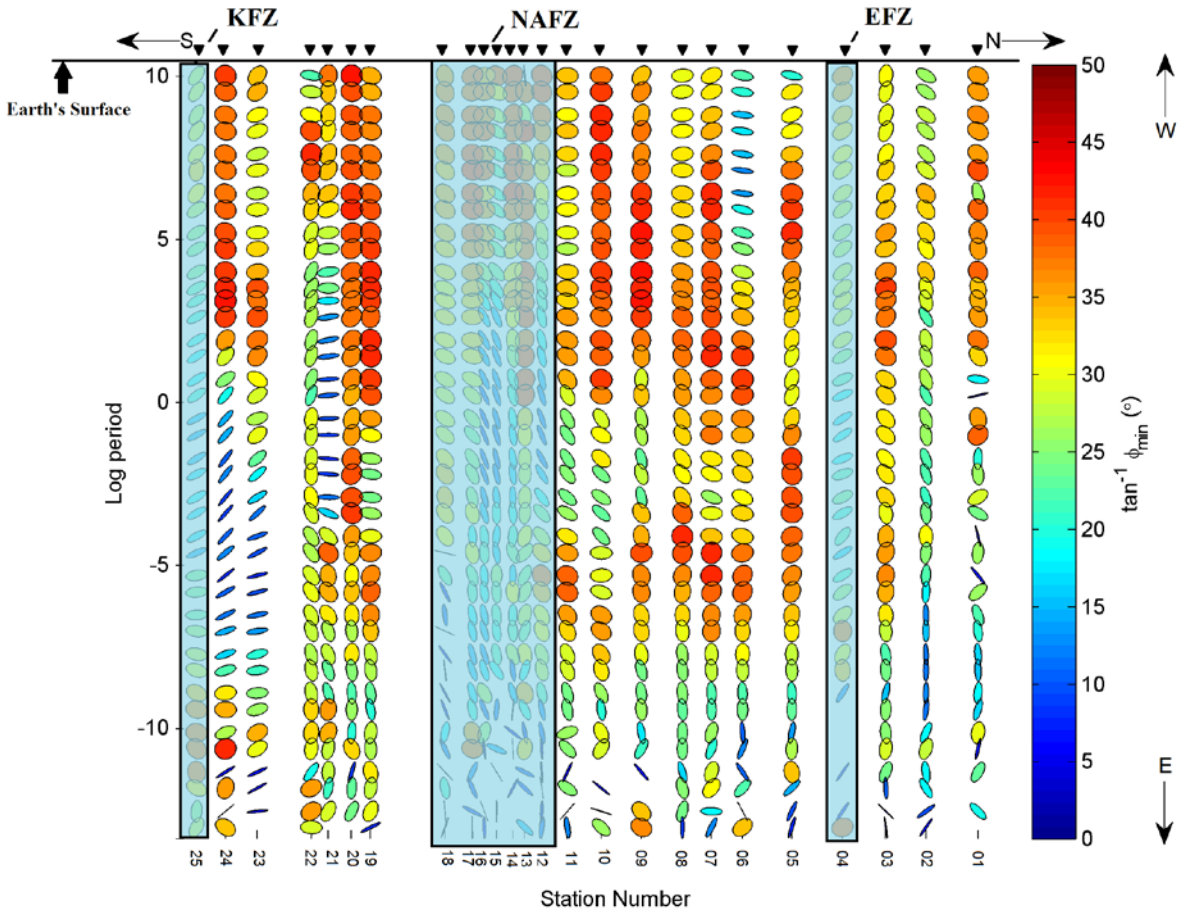

Figure 4.10. Interpreted version of the figure 4.10. Ellipses are shown in bird's-eye view and major axis directions are in the same direction with geographical N-S-E-W. Blue windows correspond the geological structures. From right to left, first window correspond to Ekinveren Fault zone (EFZ), second one correspond to the NAFZ, the the last one corresponds to Kızılırmak Fault zone (KFZ). Black triangles represent MT sounding locations.

5. DISCUSSION

Interpretation of relatively longer period MT data that often involve distortion effects caused by near surface heterogeneities is difficult. Traditional solution for this difficulty is to assume a simplified 2D structure for underlying regional conductivity distribution. The advantage brought by the phase tensor, reduces the importance of some of the assumptions made in the MT method. That is purely because the horizontal components of the electric and the magnetic fields can be derived directly, without being concerned by the effects of the distortions.

The most prominent advantage of the phase tensor is to get rid of distortions by using simple algebraic processes. Whereas the other conventional distortion removal and strike determination methods are time consuming and include more complicated processes, the phase tensor method can be applied in simple terms.

The major axis of the phase tensor ellipses shows the preferred direction of induced current. If the structure under the surface is conductive, ellipses have radial alignment. On the other hand, if the structure is resistive, ellipses have tangential alignment to the structure. Azimuth (α - β) of the major axis of the ellipse controls the ellipse alignment. In other words, azimuth controls the flow direction. Also, the skew angle (β), determines the dimensionality of the basement that is investigated. Phase tensor method reflects galvanic distortion at near surface and it reflects any change in the conductivity at deeper levels. The phase tensor method can be used to detection of the deeper conductivity changes.

Normally, results of modeling should have more consistency with results of Caldwell et al. (2004). Because of the difference between modeling algorithms a certain part of results were consistent. Nonetheless, results in this piece of work were satisfactory. In the original work of Caldwell et al. (2004) there is no information about the three-dimensional mesh used, about the forward modeling details or the code itself.

Phase tensor method has been applied to observed data set. Responses of the data were shown on figures from 4.6 to 4.10. That observed data were modeled by sophisticated three-dimensional inversion algorithm to create resistivity model by Tank et al. (2014). This resistivity model is presented in Figure 5.1. Results of the phase tensor method and the resistivity model are consistent. As can be seen from the figure, a transformation from conductor to resistor occurred under the fourth station. Also, the phase tensor ellipses show a boundary at the fourth station. That is, ellipses align radially to conductive side. By looking resistivity model from Tank et al., (2014), it is very clear that NAFZ behaved as a barrier for fluids. At the north side of the NAFZ, a conductor occurred and the NAFZ blocked it. That explains the barrier nature of the NAFZ. Similarly, this barrier nature of the NAFZ can be seen from the phase tensor ellipse pseudo-section (figures 4.9 and 4.10). Color of ellipses showed that the conductivity changed with depth in the pseudo-section (Figure 4.10). At the NAFZ, ellipse colors indicate conductivity near the surface and indicate resistivity at depth. When taking into consideration of the ellipse colors, again results are consistent. At the southernmost station, the ellipses and the resistivity model of Tank et al. (2014) supports each other very well.

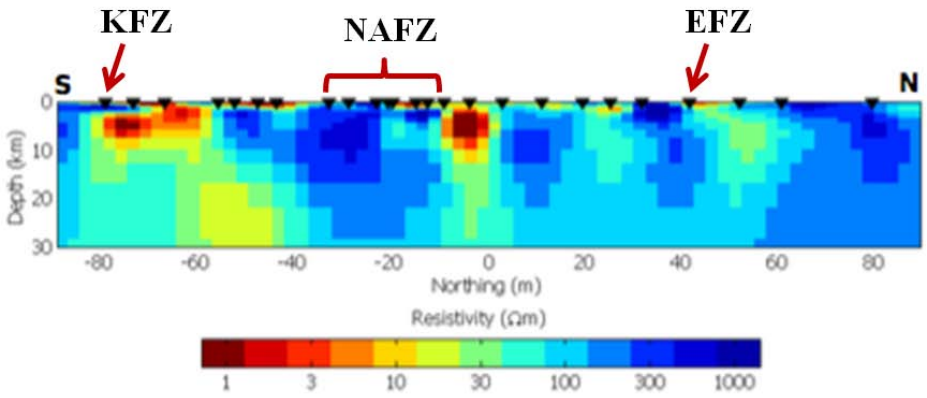

Figure 5.1: 3-D resistivity model from Tank et al.,(2014). EFZ ; Ekinveren Fault Zone, NAFZ; North Anatolian Fault Zone and KFZ; Kızılırmak Fault Zone. Black triangles show location of measurement sites.

In addition, apparent resistivity models, Figure 5.2, were used for comparison. In Figure 5.2, apparent resistivity variation depending on period is represented. Similarly, phase tensor pseudo-sections (Figures 4.9 and 4.10) represent the conductivity variation with period. Resistive and conductive areas in phase tensor pseudo sections coincide with resistive and conductive areas in apparent resistivity models (rhoxy, rhoyx). At most periods, consistency of phase tensor results (Figures 4.9 and 4.10) and apparent resistivity models (rhoxy, rhoyx) are well.

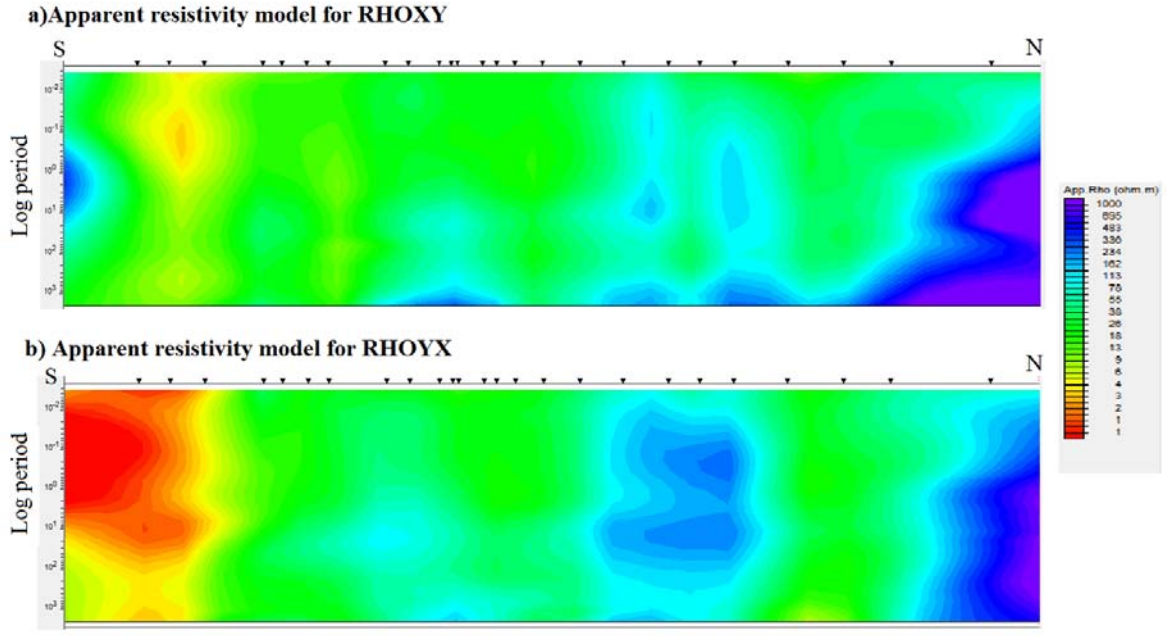

Figure 5.2: Apparent resistivity models for field data. a) Apparent resistivity model for RHOXY and b) Apparent resistivity model for RHOYX. Black triangles show MT sounding locations.

Yolsal-Çevikbilen et al. (2012) have studied the central NAFZ, too. They have investigated the region by using seismic tomography. This study focused in a larger area with north-south and east-west cross sections (Yolsal-Çevikbilen et al., 2012). Their 9th north-south cross-section matches with the MT profile that used in this study.

On Figure 5.3, Vp tomography cross-section of the 9th cross-section of Yolsal-Çevikbilen et al. (2012) is represented. According to this cross-section, Vp values were not high from the depth of 0 to 5 km. Below 5 km P wave velocity appears higher until 20 km. From 20 km to 40 km P wave velocities reach the highest values. According to their result,

Vp values increase from the depth of 5 km (especially under the surface trace of the NAFZ at depths between 5 and 25 km). Similarly, Vp values increase under the surface trace of KFZ at depths between 5 and 15 km. Moreover, in Vp/Vs tomography map, some Vp/Vs values changes from south to north near the surface and these reaches at some depth. According to Yolsal-Çevikbilen et al., (2012), that may be caused by geologic formation. In Vp/Vs tomography maps, high Vp/Vs values correspond to areas including fluid. Comparing with the resistivity model developed by Tank et al., (2014) with tomography cross-sections of Yolsal-Çevikbilen et al., (2012) are not consistent. At resistivity model, a prominent conductor appears at the north of the NAFZ, but on the tomography cross-sections, high Vp and/or high/low Vp/Vs values appear beneath the NAFZ. Seismic tomography information provided by Yolsal-Çevikbilen et al., (2012) fails to represent the NAFZ as a boundary for seismic velocities, where as the resistivity model points out that the NAFZ zone is a clear boundary for the electrical structure. Phase tensor ellipses and the colors filling them indicate variation of conductivity with depth (Figure 4.10). Resistivity model of Tank et al., (2014) and the phase tensor figures provided by the current study show good consistency.

Results of tomography cross-sections and resistivity model show some consistency for under the surface trace of KFZ. For instance, a thin horizontal resistive structure occurs under the KFZ at resistivity model from Tank et al., (2014). On the other hand, similar structure (such as low Vp/Vs valued area under KFZ) is not clear at Vp/Vs tomography from Yolsal- Çevikbilen et al., (2012). The phase tensor ellipse colors support resistivity model taken from Tank et al., (2014).

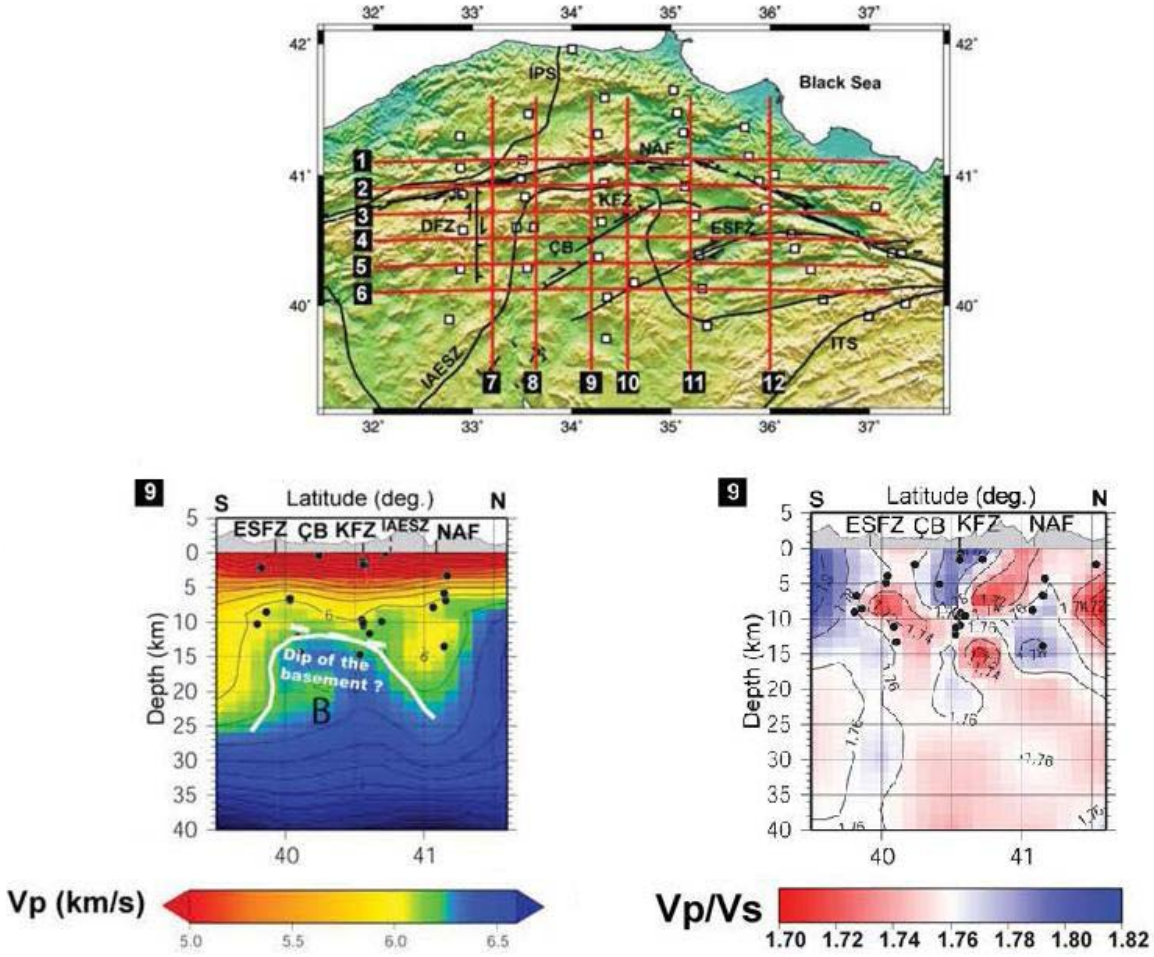

Figure 5.3: Vp and Vp/Vs tomography cross-sections for the 9th line from Yolsal-Çevikbilen et al., (2012).

Using the phase tensor method can be more practical compared to Bahr's parameters and Groom and Bailey's decomposition in some manners. These two conventional methods need some assumptions such as assuming the regional conductivity structure as 2D. Direction and shape of ellipses give ideas about strike and dimensionality of the subsurface. Even if Groom and Bailey's method and Bahr's parameters can be represented graphically, visualization of the phase tensor method presents clearer results compared to these two approaches.

6. CONCLUSION

In that study, MATLAB® scripts were developed for the interpretation of MT data as phase tensor ellipses. The scripts were tested by means of creating three-dimensional synthetic models as well as observed models. Synthetic models were constructed with RM3D code developed by Mackie et al. (1993). MATLAB® scripts were used plotting phase tensor ellipses and pseudo-sections. Observed data collected at the central North Anatolian Fault Zone near Tosya, Kastamonu were used and their results were presented. Results of this attempt were compared with other geophysical survey results performed at a close by area. Clear resemblances were found and pointed out.

APPENDIX A- BRIEF INFORMATION ABOUT TENSORS AND FORWARD MODELING

A.1. TENSORS

A.1.1. Description of a Tensor

A tensor can be described by arrays of functions. Each function of such an array is called a component and these components are functions of the selected coordinate systems. Tensors are independent of the coordinate system. That property makes tensors useful objects for representing some laws and applications in science and engineering. Generally, scalars are referred to as tensors with rank zero where vectors are referred to as tensors with rank one (Hadsell, 1995; Heinbockel, 2001).

A.1.1. Some Basic Operations of Tensors

The algebraic operation of addition or subtraction can be applied to systems of the same type and rank. For example, suppose that A and B are 2x2 tensors, subtraction and addition operations can be applied to them. Such as;

$$A = \begin{bmatrix} a_{11} & a_{12} \\ a_{21} & a_{22} \end{bmatrix} \text{ and } B = \begin{bmatrix} b_{11} & b_{12} \\ b_{21} & b_{22} \end{bmatrix} \quad \text{(A.1.)}$$

$$A + B = \begin{bmatrix} a_{11} + b_{11} & a_{12} + b_{12} \\ a_{21} + b_{21} & a_{22} + b_{22} \end{bmatrix} \quad \text{(A.2.)}$$

A.1.2. Why Do We Use Tensors?

- Tensors and their analysis may be applied to N-dimensional hyperspaces.
- Scientific concepts, which require functions to express, can be formulated easily.
- The classical analysis is embedded in the tensor analysis.
- Results are translated easily to forms appropriate to any coordinate system.
- Physical concepts can be expressed without reference to any particular coordinate system (Hadsell, 1995).

A.1.3. Relationship to the MT Phase Tensor

Representation of the MT phase takes the form of a second-rank tensor. The phase tensor components and their associated three coordinate invariants are simple functions of the observed impedance tensor components. The MT phase tensor can be visualized as an ellipse where the principal values of the tensor correspond to the major and minor axes of the MT phase tensor ellipse (Caldwell et al., 2004).

A.2. FORWARD MODELING

The typical target of modeling operations is to understand the behavior of the system that is studied from physical point of view. That is, modeling operations are used for describing to a phenomenon that affects the whole system. Mainly, forward modeling is construction of a theoretical model, which allows to predict observed effects by means of computational techniques. Also it allows to predict the results of any possible measurement. The solution of the forward problem provides a relation between the parameters used to describe the model (m) and quantities (d) that can be measured

$$d = G(m) \qquad \text{(A.3.)}$$

which quantifies the model prediction (Tarantola, 2005; Debski, 2010).

APPENDIX B – TEST OF THIS STUDY

In order to test the health of the MATLAB® scripts, a comparison has been performed between MATLAB® scripts developed in this study and a script developed by Jones (2006) that includes a Fortran executable, “mtphasetensor”, for calculating the phase tensors and GMT (Generic Mapping Tools) script for imaging them. This Fortran program calculates the parameters of the phase tensor ellipses by reading j-format files and then it writes calculation results in files for every station. After combining every result in a single file for every different frequency, ellipses were drawn in GMT. GMT shell script, which is written by Ryokei Yoshimura in 2005 (personal communication), was used to understand how to draw a phase tensor ellipse in GMT, then a GMT shell script was written in order to draw ellipses for data from Jones (2006) Fortran executable. Although the difference between Jones (2006) Fortran executable and our MATLAB® scripts the consistency of the results are satisfactory. Results from GMT were shown in Figure 5.5. At high frequency, in Figure 5.5.a, again shapes of ellipses are similar with results of MATLAB® and Caldwell et al. (2004). At middle frequency, in Figure 5.5.b, shapes of ellipses are similar with results of MATLAB® scripts. At low frequency, in Figure 5.5.c, shapes of the ellipses are similar with results of MATLAB® scripts.

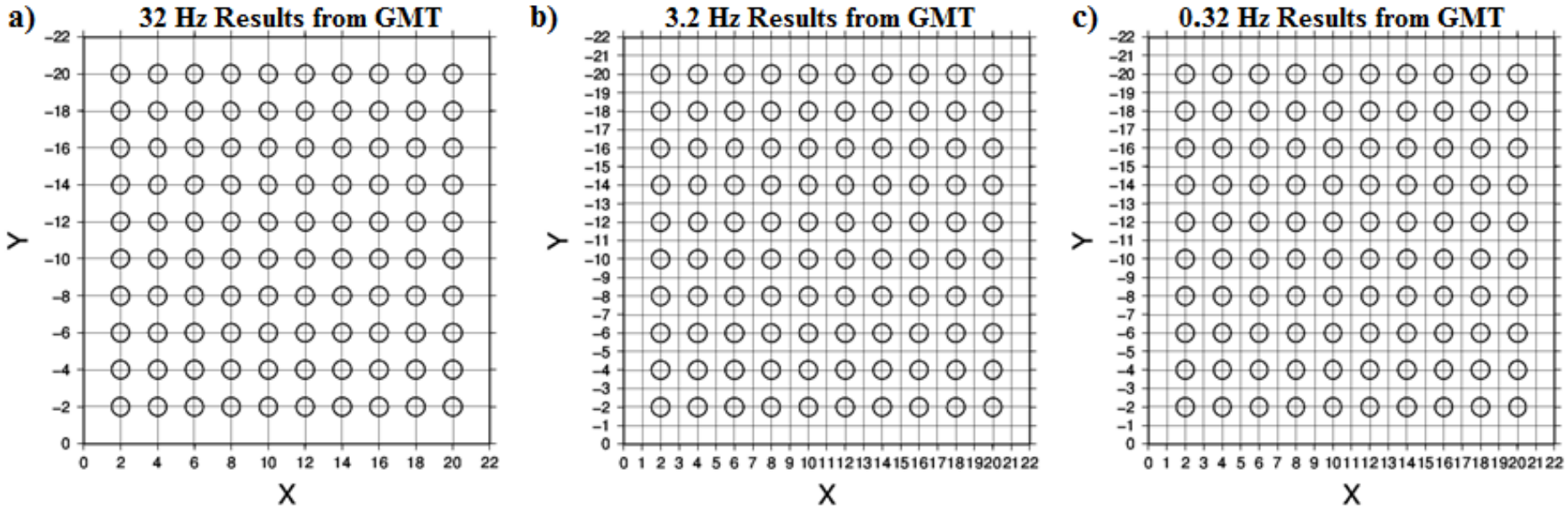

Figure B.1: Map of phase tensor ellipses at three different frequencies [a)32hz b)3.2hz c)0.32hz] for the model shown in figure 3.1. Calculation of parameters was done in Jones (2006) Fortran executable and drawings were done in GMT.

APPENDIX C - PHASE TENSOR ELLIPSE MAPS FOR OTHER PERIODS

In this appendix, phase tensor ellipse results from real data will be shown. These results are belong to other 17 periods,which were chosen randomly, from top to bottom.

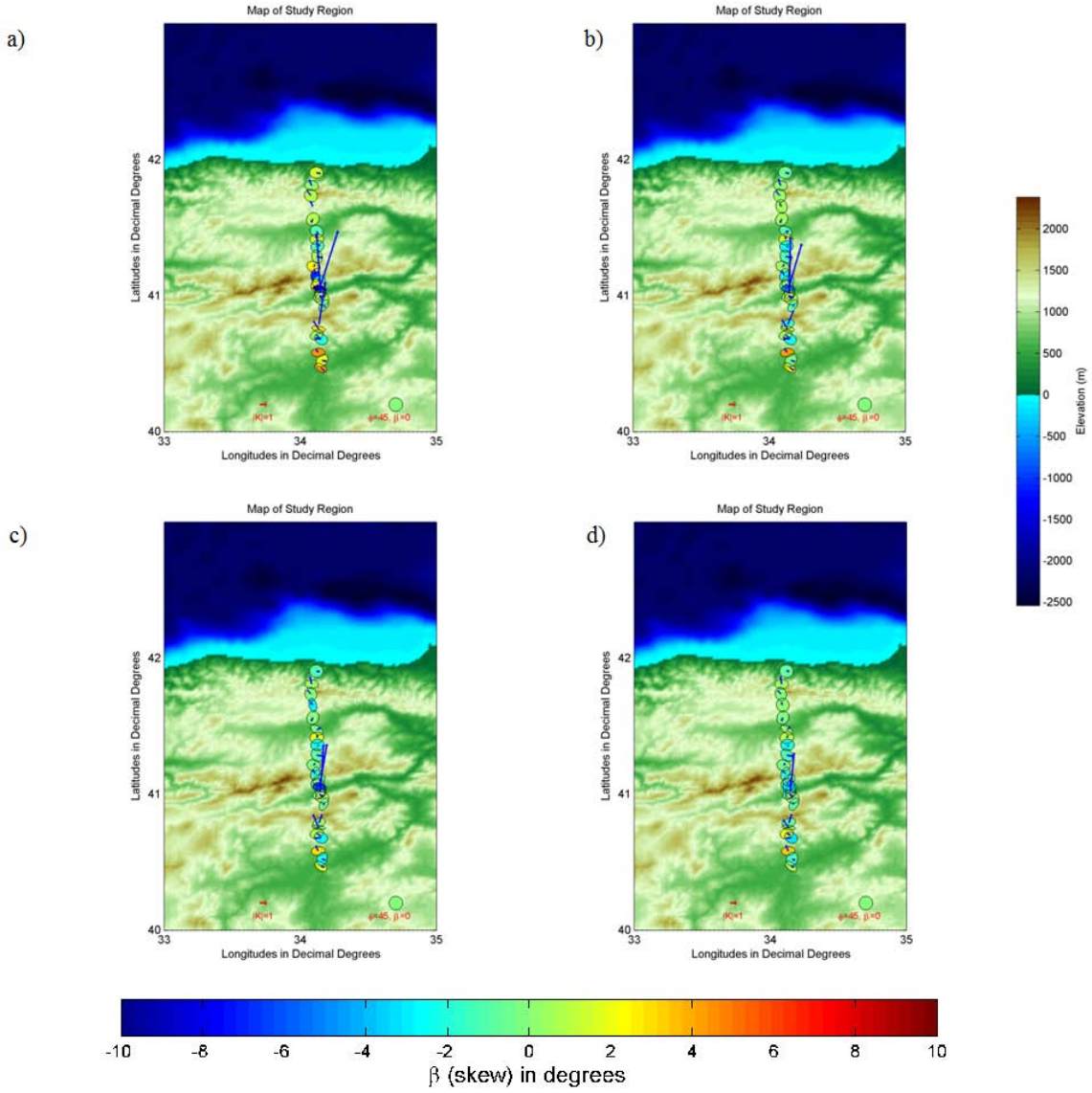

Figure C.1.: Phase tensor maps of real data at a) 0.003 sec. b) 0.004 sec. c) 0.006 sec d) 0.008 sec.

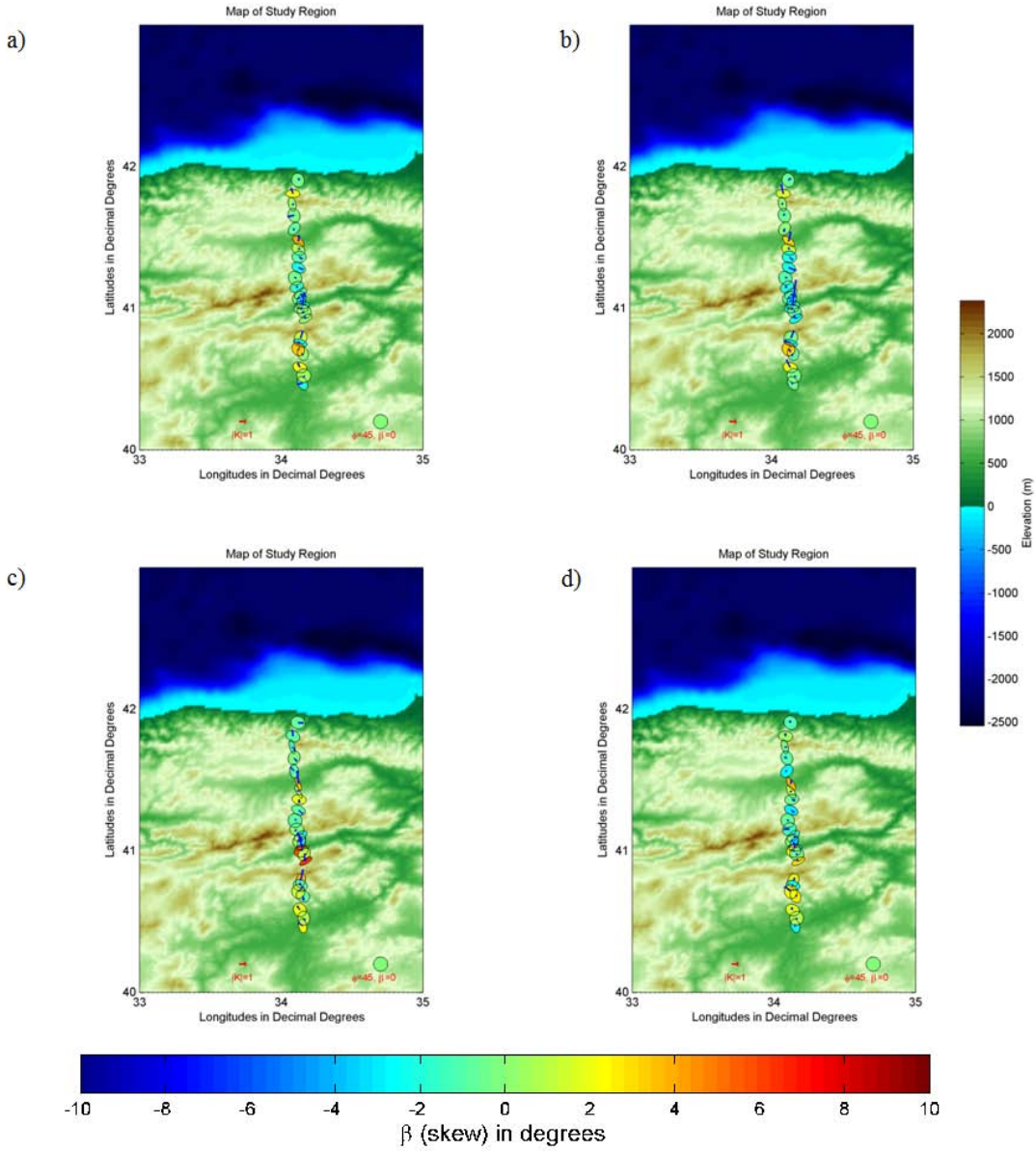

Figure C.2.: Phase tensor maps of real data at a) 0.06 sec. b) 0.05 sec. c) 0.3 sec d) 0.13 sec.

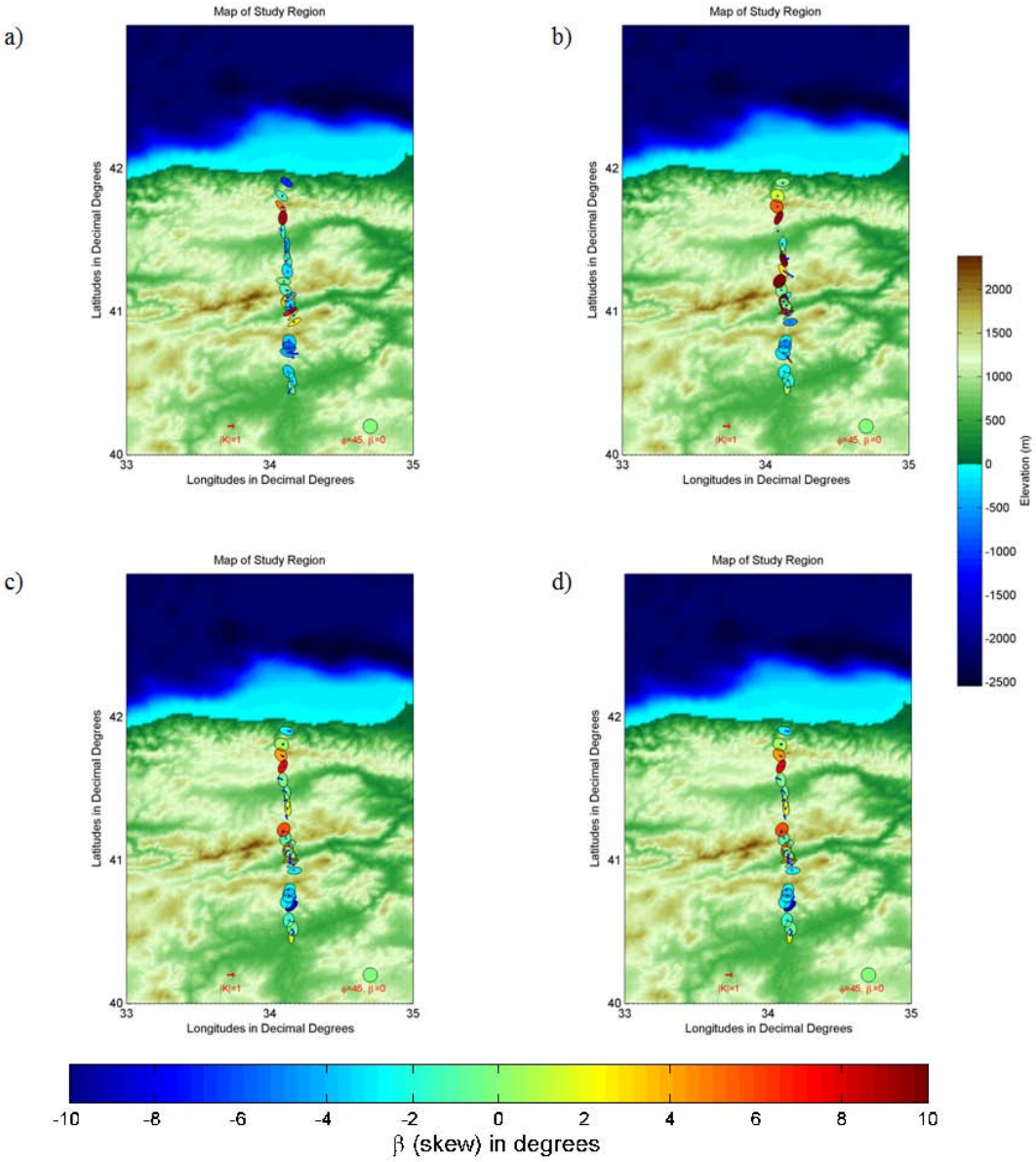

Figure C.3.: Phase tensor maps of real data at a) 5 sec. b) 21 sec. c) 28 sec d) 42 sec.

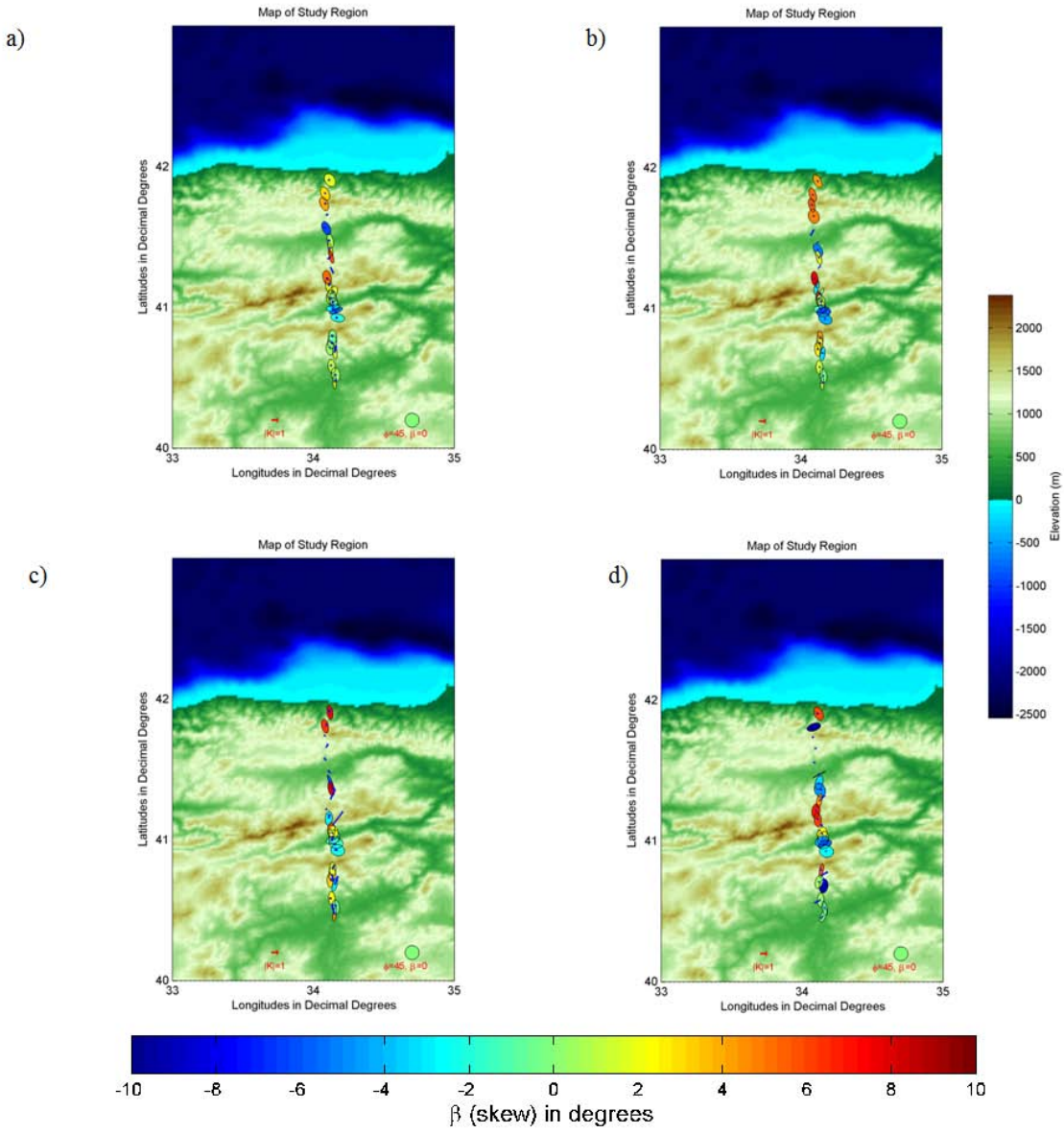

Figure C.4.: Phase tensor maps of real data at a) 85 sec. b) 169 sec. c) 227 sec d) 34 sec.

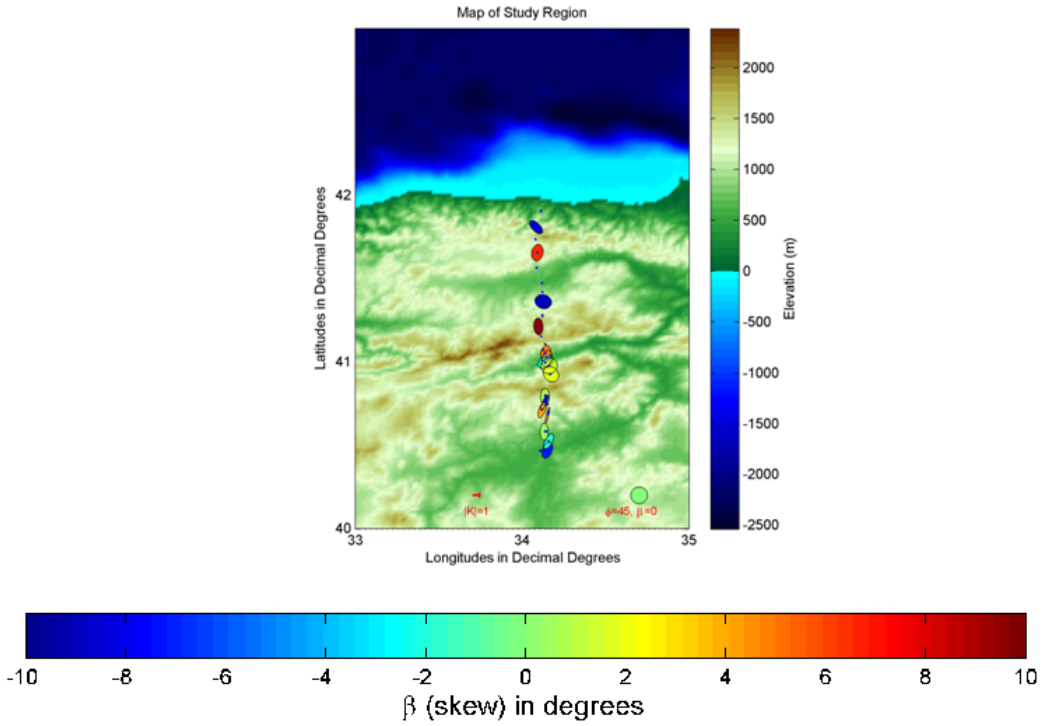

Figure C.5.: Phase tensor map of real data at 454 sec.

APPENDIX D – MATLAB SCRIPTS

D.1. pt_par_cal.m

pt_par_cal.m (phase tensor parameter calculation) calculates phase tensor method parameters and applies normalization to maximum and minimum phases depending on maximum phase value. In order to use this script, one should have a text formatted impedance file (impedance file also contains tipper values). Impedances should be separated by columns (4 real part columns and 4 imaginary part columns and also 2 tipper real parts, 2 tipper imaginary parts). This script uses the function phasetensor1.m and it will be represented. After calculating parameters, it writes them to a file as “filename_pt_nor.txt”.

```
clear all;
close all;
clc;
format long
dosya=load('filename.txt');
 [k,l]=size(dosya);
X11=dosya(:,2);
X12=dosya(:,4);
X21=dosya(:,6);
X22=dosya(:,8);
Y11=dosya(:,3);
Y12=dosya(:,5);
Y21=dosya(:,7);
Y22=dosya(:,9);
```

```
for i=1:k;

[pt(:,:,i),a(i),b(i),c(i),d(i),e(i)]=phasetensor1(X11(i),X12(i),X21(i),X22(i),Y11(i),Y12(i),Y21(i),Y22(i));

end

s=[];

s(:,1)=a; s(:,2)=b; s(:,3)=c; s(:,4)=d; s(:,5)=e;

s=[s(:,1) s(:,2) s(:,3) s(:,4) s(:,5)];

dlmwrite('filename_pt_nor.txt',s,'delimiter','\t','precision','%.8f')
```

D.2. phasetensor1.m

This is a function and originally it calculates parameters of the phase tensor method.

```
function[phi,phimax,phimin,alpha,beta,aminb]=phasetensor1(X11,X12,X21,X22,Y11,Y12,Y21,Y22)

format long

X=[X11 X12 ;X21 X22];

Y=[Y11 Y12; Y21 Y22];

de_X=X(1,1)*X(2,2)-X(2,1)*X(1,2); %determinant of X

%constructing phase tensor by finding inverse of X dot Y

phi(1,1)=(1/de_X)*(X(2,2)*Y(1,1)-X(1,2)*Y(2,1));

phi(1,2)=(1/de_X)*(X(2,2)*Y(1,2)-X(1,2)*Y(2,2));

phi(2,1)=(1/de_X)*(X(1,1)*Y(2,1)-X(2,1)*Y(1,1));

phi(2,2)=(1/de_X)*(X(1,1)*Y(2,2)-X(2,1)*Y(1,2));

phi=[phi(1,1) phi(1,2); phi(2,1) phi(2,2)]; % phase tensor
```

```
%calculating determinant, skew and trace
detr= phi(1,1)*phi(2,2) - phi(1,2)*phi(2,1); %determinant
tr= phi(1,1)+phi(2,2); %trace
sk= phi(1,2)-phi(2,1); % skew
%calculating alpha and beta
 alp = (0.5 * atan2( (phi(1,2)+phi(2,1)),(phi(1,1)-phi(2,2)))); % alpha
 bet  = (0.5 * atan2( (phi(1,2)-phi(2,1)),(phi(1,1)+phi(2,2)))); %beta (skew angle)
alpha=rad2deg(alp);
beta=rad2deg(bet);
aminb=alpha-beta;
phi1 = tr/2;
phi2=sqrt(detr);
phi3 = sk/2;
psi1= (0.5 *sqrt( ((phi(1,2)+phi(2,1))^2) +((phi(1,1)-phi(2,2))^2)));
psi2= (0.5 *sqrt( ((phi(1,2)-phi(2,1))^2) +((phi(1,1)+phi(2,2))^2)));
phimax1=psi1+psi2;
phimin1=psi2-psi1;
phimax=phimax1/phimax1;
phimin=phimin1/phimax1;

end
```

D.3. elps_map.m

This script uses output of pt_par_cal.m and the impedance-tipper file and plots the phase tensor ellipses and induction arrows superimposed on a topography map. In addition, it saves the output as a png file.

```
clear all;close all;clc;
dosya=load('filename_pt_nor.txt')
dosya2=load ('filename.txt')
% defining pt ellipse parameters
pmax=dosya(:,1);
pmin=dosya(:,2);
alp=dosya(:,3);
bet=dosya(:,4);
aminb=dosya(:,5);
[m,n]=size(dosya);

% defining induction arrow parameters from tipper values
tx_real=dosya2(:,10);
tx_ima=dosya2(:,11);
ty_real=dosya2(:,12);
ty_ima=dosya2(:,13);
% topography map of study area
etopo=load ('area_topography.asc');
dots=load ('coordinates.txt');
etopo=flipud(etopo);
etopo(find(etopo==-32768))=NaN;
a=max(etopo(:));
b=min(etopo(:));
[lon,lat]=meshgrid(33:1/60:35,40:1/60:43,0);

surf(lon,lat,etopo);
```

```
shading interp;

axesm mercator;

zlimits=([b a]);

demcmap(etopo);

c1=colorbar;

view(0,90);

title('Map of Study Region');

xlabel('Longitudes in Decimal Degrees');

ylabel('Latitudes in Decimal Degrees');

ylabel(c1,'Elevation (m)');

set(gca,'XTick',[32:1:36]);

set(gca,'YTick',[40:1:42]);

% phase tensor ellipses and induction arrows plot part

hold on;

aminb(aminb<-90)=aminb(aminb<-90)+180;

aminb(aminb>90)=aminb(aminb>90)-180;


for i=1:m;

    %phase tensor construction by svd

    r1(:,:,i)=[cosd(aminb(i)) sind(aminb(i));-sind(aminb(i)) cosd(aminb(i))];

    r2(:,:,i)=[cosd((aminb(i)+2*bet(i)))  sind((aminb(i)+2*bet(i)));-sind((aminb(i)+2*bet(i)))
cosd((aminb(i)+2*bet(i)))];

    pt(:,:,i)=r1(:,:,i)'*[pmax(i) 0; 0 pmin(i)]*r2(:,:,i);

    ptel(:,:,i)=pt(:,:,i)*[cosd(0:1:360); sind(0:1:360)];

   % normalizing tipper values for better induction arrows

 txyrn=sqrt((max(tx_real))^2+(max(ty_real))^2);
```

```
step=0.1;

minval=-10;

maxval=10;

cmap=jet((maxval-minval)/step);


% plotting pt ellipses on topography map and setting skew angle boundaries

 if bet(i)>10 && bet(i)<-10

    i=i+1;

  elseif bet(i)<=10 && bet(i)>=-10


fill3(((ptel(2,:,i)/20)+dots(i,2)),((ptel(1,:,i)/20)+dots(i,1)),ones(361)*4800,cmap(floor((bet(
i)-minval)/step)+1,:));

end

%plotting induction arrows

a=quiver3(dots(i,2),dots(i,1),4800,-(ty_real(i)/txyrn)./20,-
(tx_real(i)/txyrn)./20,1,'b','MaxHeadSize',0.1);

set(a,'LineWidth',1.5);

end

%induction arrow legend

a3=quiver3(33.7,40.2, 4800,(1/1)/20,(0/1)/20,1,'r');

set(a3,'LineWidth',1.5);

%phase tensor legend

fill3((1*cosd(0:1:360)./20)+34.7,(1*sind(0:1:360)./20)+40.2,ones(361)*4800,cmap(floor((
0-minval)/step)+1,:));

text(34.5,40.1,4800,'\phi=45, \beta=0','color','r','Fontsize',8);

text(33.65,40.1,4800,'|K|=1','color','r','Fontsize',8);

print('t85s_map','-dpng','-r300');
```

REFERENCES

Aygül, M., A. I., Okay, R. O., OBERHÄNSLI, M. A., Ziemann, 2015, "Thermal structure of low-grade accreted Lower Cretaceous distal turbidites, the Central Pontides, Turkey: insights for tectonic thickening of an accretionary wedge", *Turkish Journal of Earth Sciences*, Vol. *24*(5), p. 461.

Bahr, K., 1988, "Interpretation of the Magnetotelluric Impedance Tensor: Regional Induction and Local Telluric Distortion", *J. Geophys.*, Vol. 62, pp. 119-127.

Bahr, K., 1991, "Geological noise in magnetotelluric data: a classification of distortion types", *Physics of the Earth and Planetary Interiors*, Vol. 66(1), pp. 24-38.

Barka, A., 1992, "The North Anatolian Fault Zone", *Annales Tectonicae*, Vol. 6, pp. 164195.

Bedrosian, P., 2007, "MT + Integrating Magnetotellurics to Determine Earth Structure, Composition and Processes", *Surveys in Geophysics*, Vol. 28, pp. 121-167.

Berdichevsky, M.N., V.I. Dmitriev, and E.E. Pozdnjakova, 1998, "On Two-Dimensional Interpretation of Magnetotelluric Soundings", *Geophys. J. Int.*, Vol. 133, pp. 585606.

Bibby, H. M., 1986, "Analysis of multiple-source bipole-quadripole resistivity surveys using the apparent resistivity tensor", *Geophysics*, Vol. 51(4), pp. 972-983.

Bibby, H. M., T. G., Caldwell & C. Brown, 2005, "Determinable and non-determinable parameters of galvanic distortion in magnetotellurics", *Geophysical Journal International*, Vol. *163*(3), pp. 915-930.

Booker, J. R., 2014, "The magnetotelluric phase tensor: a critical review", *Surveys in Geophysics*, Vol. 35(1), pp. 7-40.

Cagniard, L., 1953, "Basic Theory of the Magnetotelluric Method in Geophysical Prospecting", *Geophysics*, Vol. 18, pp. 605-635.

Caldwell, T. G., H. M., Bibby & C. Brown, 2004, "The magnetotelluric phase tensor", *Geophysical Journal International*, Vol. *158*(2), pp. 457-469.

Chave, A. D., & A. G., Jones, 2012, *"The magnetotelluric method: Theory and practice*", Cambridge University Press.

Espurt, N., J. C., Hippolyte, N., Kaymakci, & E., Sangu, 2014, "Lithospheric structural control on inversion of the southern margin of the Black Sea Basin, Central Pontides, Turkey", *Lithosphere*, Vol. 6(1), pp. 26-34.

Groom, R.W., and, R.C. Bailey, 1989, "Decomposition of Magnetotelluric Impedance Tensor in the Presence of Local Three-Dimensional Galvanic Distortion", *J. Geophys. Res.*, Vol. 94, pp. 1913-1925.

Hadsell, F., 1995, "Tensors of geophysics for mavericks and mongrels", R. W. Wiley (Ed.). Tulsa: Society of Exploration Geophysicists.

Heinbockel, J. H., 2001, "Introduction to tensor calculus and continuum mechanics", Vol. 52, Trafford.

Heise, W., H. M., Bibby, T. G., Caldwell, S. C., Bannister, Y., Ogawa, S., Takakura, & T., Uchida, 2007, "Melt distribution beneath a young continental rift: the Taupo Volcanic Zone, New Zealand", *Geophysical Research Letters*, Vol. 34(14).

Hill, G. J., T. G., Caldwell, W., Heise, D. G., Chertkoff, H. M., Bibby, M. K., Burgess, and R. A., Cas, 2009, "Distribution of melt beneath Mount St Helens and Mount Adams inferred from magnetotelluric data", *Nature Geoscience*, Vol. 2(11), pp. 785-789.

Jones, A. G., 1999, "Imaging the Continental Upper Mantle Using Electromagnetic Methods", *Lithos*, Vol. 48, pp. 57-80.

Kaufman A. A. and G.V. Keller, 1981, *The magnetotelluric sounding method, methods in geochemistry and geophysics*, Elsevier scientific publishing company.

Keller, G. V., & F. C., Frischknecht, 1966, Electrical methods in geophysical prospecting.

Mackie, R. L., T. R., Madden, & P. E., Wannamaker, 1993, "Three-dimensional magnetotelluric modeling using difference equations-Theory and comparisons to integral equation solutions", *Geophysics*, Vol. 58(2), pp. 215-226.

McNeice, G.W., and A.G., Jones, 2001, "Multisite, Multifrequency Tensor Decomposition of Magnetotelluric Data", *Geophysics*, Vol. 66, pp. 158-173.

Okay, A. I., & O., Tüysüz, 1999, "Tethyan sutures of northern Turkey", *Geological Society, London, Special Publications*, Vol. 156(1), pp. 475-515.

Okay, A. I., O., Tüysüz, M., Satır, S., Özkan-Altiner, D., Altiner, S., Sherlock, & R. H., Eren, 2006, "Cretaceous and Triassic subduction-accretion, high-pressure–low-temperature metamorphism, and continental growth in the Central Pontides, Turkey", *Geological Society of America Bulletin*, Vol. 118(9-10), pp. 1247-1269.

Okay, A. I., G., Sunal, S., Sherlock, Altıner, D., O., Tüysüz, A. R., Kylander-Clark, and M., Aygül, 2013, "Early Cretaceous sedimentation and orogeny on the active margin of Eurasia: Southern Central Pontides, Turkey" *Tectonics*, Vol. 32(5), pp. 1247-1271.

Park, S.K., G.P. Biasi, R.L. Mackie, and T.R. Madden, 1991, "Magnetotelluric Evidence for Crustal Suture Zones Bounding the Southern Great Valley, California", *Journal of Geophysical Research*, Vol. 96, pp. 353-376.

Parkinson, W.D., 1962, "The Influence of Continents and Oceans on Geomagnetic Variations", *The Geophysical Journal of the Royal Astronomical Society*, Vol. 6, pp. 411-449.

Reynolds, J.M., 1997, *An Introduction to Applied and Environmental Geophysics*, John Wiley and Sons, Inc., Newyork.

Rikitake, T., 1948, "Notes on the Electromagnetic Induction within the Earth".

Ritter, O., A. Hoffmann-Rothe, P. A. Bedrosian, U. Weckmann and V. Haak, 2005, "Electrical Conductivity Images of Active and Fossil Fault Zones", *The Geological Society of Londan, special Publications*, Vol. 245, pp. 165-186.

Simpson, F. and K. Bahr, 2005, *Practical Magnetotellurics*, Cambridge University Press.

Sadiku, N. O., 2001, "Numerical methods in Electromagnetics", *Mathew, Boca Raton, London, New York, Washington DC.*

Swift C. M., 1967, *A Magnetotelluric Investigation of an Electrical Conductivity Anomaly in the South-Western United States,* Ph.D. Thesis, M.I.T.

Tank, B., B., Yakar, Ö., Cengiz, E. A., Sandvol, and Y., Ogawa, 2014, "Determining the Role of Fluids near a Slab Window in Central Anatolia, Turkey by Magnetotellurics Method", In *AGU Fall Meeting Abstracts,* Vol. 1, p. 3669.

Tarantola, A., 2005, "Inverse problem theory and methods for model parameter estimation", siam.

Tikhonov, A.N., 1950, "On Determining Electrical Characteristics of the Deep Layers of the Earth's Crust", *Doklady,* Vol. 73, pp. 281-285.

Vozoff, K., 1972, "The Magnetotelluric Method in the Expolaration of Sedimentery Basins", *Geophysics*, Vol. 37, pp. 98-141.

Vozoff, K., 1991, "The Magnetotelluric Method", in Nabighian, M. N., Ed., Electromagnetic Methods in Applied Geophysics: SEG., *2B*, 641-711.

Ward, Stanley H., and G. W., Hohmann, 1988, "Electromagnetic Theory for Geophysical Applications", *Electromagnetic Methods in Applied Geophysics,* Vol. 1, pp. 130311.

Yolsal-Çevikbilen, S., C. B., Biryol, S., Beck, G., Zandt, T., Taymaz, H. E., Adiyaman, and A. A., Özacar, 2012, "3-D crustal structure along the North Anatolian Fault Zone in north-central Anatolia revealed by local earthquake tomography", *Geophysical Journal International*, Vol. 188(3), pp. 819-849.